Investigating the role of typhoon-induced gravity waves and stratospheric hydration in the formation of tropopause cirrus clouds observed during the 2017 Asian monsoon

Amit Kumar Pandit[1], Jean-Paul Vernier[1,2], Thomas Duncan Fairlie[2†], Kristopher M. Bedka[2], Melody A. Avery[2], Harish Gadhavi[3], Madineni Venkat Ratnam[4], Sanjeev Dwivedi[5], Kasimahanthi Amar Jyothi[6], Frank G. Wienhold[7], Holger Vömel[8], Hongyu Liu[1,2], Bo Zhang[1,2], Buduru Suneel Kumar[9*], Tra Dinh[10], and Achuthan Jayaraman[11]

[1]National Institute of Aerospace, Hampton, USA
[2]NASA Langley Research Center, Hampton, USA.
[3]Physical Research Laboratory, Ahmedabad, India.
[4]National Atmospheric Research Laboratory, Gadanki, India.
[5]Meteorological Centre, India Meteorological Department, Ministry of Earth Sciences, Bhubaneswar, India.
[6]National Centre for Medium Range Weather Forecasting, Noida, India.
[7]ETH Zurich, Zurich, Switzerland.
[8] National Centre for Atmospheric Research, Boulder, USA.
[9]Tata Institute of Fundamental Research Balloon Facility, Hyderabad, India.
[10]Department of Physics, University of Auckland, New Zealand.
[11]Bangalore University, Bangalore, India.

† Deceased on 27 April 2022

* Deceased on 12 February 2024

Correspondence to: Amit Kumar Pandit (amitkpandit86@gmail.com)

Abstract. We investigate the formation mechanism of a tropopause cirrus cloud layer observed during the Balloon measurement campaigns of the Asian Tropopause Aerosol Layer (BATAL) over Hyderabad (17.47° N, 78.58° E), India on 23 August 2017. Simultaneous measurements from a backscatter sonde and an optical particle counter onboard a balloon flight revealed the presence of a subvisible cirrus cloud layer (optical thickness ~0.025) at the cold-point tropopause (temperature ~ -86.4 °C, altitude ~17.9 km). Ice crystals in this layer are smaller than 50 μm with a layer-mean ice-crystal number concentration of about 46.79 L^{-1}. Simultaneous backscatter and extinction coefficient measurements allowed us to estimate range-resolved lidar ratio inside this layer with a layer-mean value of about 32.18±6.73 sr which is in good agreement with earlier reported values at similar cirrus cloud temperatures. The formation mechanism responsible for this tropopause cirrus is investigated using a combination of three-dimensional back-trajectories, satellite observations, and ERA5 reanalysis data. Satellite observations revealed that the overshooting convection associated with a category-3 typhoon *Hato*, which hit Macau and Hong Kong on 23 August 2017 injected ice into the lower stratosphere. This caused a hydration patch that followed the Asian Summer Monsoon anticyclone to subsequently move towards Hyderabad. The presence of tropopause cirrus cloud layers in the cold temperature anomalies and updrafts along the back-trajectories suggested the role of typhoon-induced gravity waves in their formation. This case study highlights the role of typhoons in influencing the formation of tropopause cirrus clouds through stratospheric hydration and gravity waves.

1 Introduction

Cirrus clouds are composed of non-spherical ice crystals that exhibit high variability in their size and shapes. Optically thin cirrus coverage is highest over the tropics in a region between the top of maximum convective outflow (near 12-14 km) and the cold-point tropopause (CPT, between 16 and 18 km) called the Tropical Tropopause Layer (TTL; Randel and Jensen (2013). Due to their frequent occurrence at high altitudes and cold temperatures, and their thin-wispy structures, cirrus clouds trap long-wave terrestrial radiation more efficiently than they reflect incoming short-wave solar radiation (Lohmann and Gasparini, 2017). Therefore, high thin cirrus clouds induce a net warming impact on the climate system (Gasparini and Lohmann, 2016; Hong et al., 2016). The radiative effects of cirrus clouds depend on their macrophysical (coverage, altitude, geometrical thickness) and microphysical properties (number concentration, mass density and size and shape distributions of ice crystals) (Liou, 1986, 2005). Higher cirrus clouds have a larger warming effect on climate than those at lower levels (Lohmann and Gasparini, 2017). Simulations using General Circulation Models (GCMs) have shown that the radiative impact of cirrus clouds is sensitive to small changes in the number concentration of small ice crystals (Sanderson et al., 2008; Mitchell et al., 2008). In this context, subvisible cirrus clouds (having optical thickness less than 0.03 at visible wavelengths) occurring near the CPT are important because they are the highest type of cirrus clouds with significant horizontal coverage. Subvisible cirrus clouds can have a relatively long lifetime because they usually consist of low concentrations of small ice crystals, which are more slowly removed by sedimentation and yield greater radiative heating than larger ones, given the same ice mass (Fu and Liou, 1993).

Apart from their radiative impact, subvisible cirrus clouds play an important role in regulating the water vapour in the upper troposphere and lower stratosphere (UTLS) region through dehydration (Jensen et al., 1996). Dehydration efficiency depends on microphysical processes such as nucleation, growth and sedimentation (Rollins et al., 2016). Understanding of microphysical processes under different dynamical forcings and their representation in GCMs remain poor due to numerous factors, one being the lack of accurate measurements of microphysical properties of ice crystals with particle sizes less than 100 µm from the current generation probes (Heymsfield et al., 2017; Baumgardner et al., 2017; Kuhn and Heymsfield, 2016). In situ measurements provide accurate information about the microphysical properties, which are essential for estimating their radiative impact on climate and for the calibration and validation of ice-cloud products from passive and active remote sensing sensors. Balloons and aircrafts are the most common in situ measurement platforms for ice crystal microphysical properties. Due to their slow ascent, balloons provide cloud vertical profiles at high resolution, unlike aircrafts which provide larger horizontal coverage but miss fine vertical information and detailed imaging of ice crystal habits. Moreover, ice measurements using balloons do not suffer as much from shattering effects and do not require corrections due to compressed air as in case of aircraft measurements under its wings (Wolf et al., 2018).

There have been several in situ measurements of tropical cirrus clouds using balloon-borne and aircraft-based instruments (Krämer et al., 2016; Jensen et al., 2017; Schoeberl et al., 2019; Krämer et al., 2020 and references therein). However, most of those measurements were over Australia, Brazil, Central America, Europe, and the Western Pacific. Only a limited number of field campaigns have occurred over the Asian Summer Monsoon

(ASM) region (Krämer et al., 2020), despite the important role played by ASM in the transport of aerosols (Vernier et al., 2015, 2018), water vapour (Nützel et al., 2019; Khaykin et al., 2022; Wang et al., 2019) and the formation of cirrus clouds (Ueyama et al., 2018) in the UTLS region. Additionally, the ASM region has the largest coverage of high-altitude cirrus and sub-visible cirrus clouds during the boreal summer (Martins et al., 2011). Field campaigns such as the Balloon measurement campaigns of the Asian Tropopause Aerosol Layer (BATAL) (Vernier et al., 2018) and aircraft campaigns such as StratoClim (Krämer et al., 2020) and the Asian Monsoon Chemical and Climate Impact Project (ACCLIP, https://www.eol.ucar.edu/field_projects/acclip) have been organized over the ASM region to understand the physical, chemical, and dynamical characteristics of the Asian Tropopause Aerosol Layer (ATAL) along with cirrus cloud microphysics.

Satellite measurements have shown that the UTLS aerosol optical depth between 13 and 18 km altitude over the ASM region has increased three-fold since the late 1990s (Vernier et al., 2015). A balloon-borne study over Tibetan Plateau (He et al., 2019) also showed evidence for the hygroscopic growth of particles inside the ATAL. These may have significant impact on the microphysics of cirrus clouds, especially subvisible cirrus clouds that occur in the proximity of CPT during the ASM (Vernier et al., 2018). In this context, long-term (1998-2013) lidar observations over a tropical station Gadanki (13.5^o N, 79.2^o E) in south India have shown an increase in the fraction of subvisible cirrus clouds (Pandit et al., 2015). Also, the StratoClim campaign measurements in July and August 2017 from Nepal have shown the presence of solid ammonium nitrate particles from surface ammonia sources (Höpfner et al., 2019), which act as efficient ice-nuclei in the presence of ammonium sulphate particles as shown in the cloud chamber experiments (Wagner et al., 2020). In general, anthropogenic activities are expected to influence the occurrence and properties of cirrus clouds by meteorological, aerosol-induced or cloud-induced changes (Kärcher, 2017). However, these changes over the ASM region, which is one of the most polluted regions of the globe, are not well known and warrant further investigations.

The UTLS region during the ASM is dominated by the complex interplay among frequent deep convection, gravity waves, and large-scale updrafts which directly and/or indirectly lead to the formation of cirrus clouds either through liquid-origin clouds or through in situ freezing mechanisms (Krämer et al., 2016). These dynamical processes directly influence the microphysical properties of cirrus clouds. For example, slow updraft leads to thinner cirrus clouds with low IWC while faster updraft leads to thicker cirrus clouds with higher IWC (Krämer et al., 2016). A study (Ueyama et al., 2018) done using a one-dimensional (vertical), time-dependent cloud microphysical model, diabatic back-trajectories, and observations of convective clouds has suggested that nearly all the enhancement of water vapour and clouds at 100 hPa level over the ASM are due to convective saturation with minimum impact from the convectively detrained ice. This is in contrast to another recent study (Wang et al., 2019) where convective lofting of ice during the ASM is found to be the most important source of water vapour at 100 hPa level in the 10-40° N region. Khaykin et al. (2022) have recently shown evidence of direct convective hydration (water vapour mixing ratio >10 ppmv) by the overshooting convection over the ASM region using StraoClim aircraft measurements. Such large-scale organized convective systems in the southern ASM anticyclone are also associated with synoptic-scale dehydration near the tropopause. In this context, the role of large-scale organized

deep convection over the East Coast of India in the formation of tropopause cirrus clouds is a subject of interest for the BATAL campaigns organized in Hyderabad (17.47° N, 78.58° E), India (see Sect. 2.1).

In addition to meso-scale deep convection, overshooting convection frequently occurs in the tropical cyclones (Romps and Kuang, 2009), especially during their intensification (Horinouchi et al., 2020). Tropical cyclones (typhoons) during the ASM have also been seen to cause dehydration near the CPT (Li et al., 2020) and hydration in the lower stratosphere (Jiang et al., 2020). Climate change is expected to strengthen and increase the occurrence frequency of such typhoons (Stocker et al., 2013). Extreme tropical convection is expected to impact TTL water vapour and cirrus clouds (Aumann et al., 2018). However, a recent climate model study (Smith et al., 2022) suggests that the role of convective ice injection to the stratospheric water vapour budget will remain constrained by large-scale temperatures in a warmer climate. Thus, it is essential to understand how such systems influence the large-scale temperature fields and hence cirrus cloud formation in the TTL. In this context, the ASM, which is influenced by frequent deep convective systems and tropical cyclones, is preferred region for studying such influence on cirrus clouds as presented here.

In the UTLS region, deep convection generates gravity waves which are known to influence the cold-point tropopause temperature, cirrus cloud formation and hence cause dehydration in the UTLS region (Schoeberl et al., 2015, 2016). Using radiosonde observations over the tropical Western Pacific region, Kim and Alexander (2015) have shown that the CPT temperature is directly modulated by the vertically propagating waves irrespective of any change in the mean upwelling. Later, Kim et al. (2016) showed ubiquitous influence of waves on the TTL cirrus clouds using airborne observations of temperature and cirrus clouds obtained over the Western Pacific during the ATTREX campaign. Several studies (Wu et al., 2015; Nolan and Zhang, 2017; Kim et al., 2009) have reported anomalies in temperature and vertical wind speed associated with semi-circular gravity waves generated from the typhoon centre propagating horizontally and vertically through the troposphere, stratosphere, and mesosphere in expanding spirals with horizontal wavelengths typically in the range of 50-500 km and periods from 1 hour to 1.6 days.

This paper presents a case study of in situ measurements of microphysical and optical properties of a tropopause cirrus cloud layer observed during the BATAL campaign using balloon-borne instruments (a backscatter sonde and an optical particle counter) capable of detecting very thin cirrus clouds consisting of ice crystals smaller than 100 µm. We also demonstrate the usefulness of combined measurements from these instruments in measuring the range-resolved lidar ratio in situ for a tropical tropopause cirrus cloud layer for the first time (to the best of our knowledge). Using back-trajectory calculations and their intersection with the convective clouds observed by radiometers on the Himawari-8 geostationary satellite, we also investigate the origin of the air masses sampled during the balloon flight. The formation mechanism and properties of tropopause cirrus clouds along the back-trajectories are examined using the satellite observations. Section 2 describes the BATAL campaign, balloon-borne instruments, satellite, and model data used in this study. Section 3 discusses the results and Sect. 4 contains the summary.

2 Data and method

2.1 BATAL campaign and general meteorological conditions

The balloon measurements were carried out under the framework of the India Space Research Organization (ISRO)-National Aeronautics and Space Administration (NASA) joint project called BATAL (Vernier et al., 2018) during August 2017 from Tata Institute of Fundamental Research Balloon Facility (TIFR-BF, https://www.tifr.res.in/~bf/) located at 17.47° N, 78.58° E, in Hyderabad, India. During the ASM period (June to
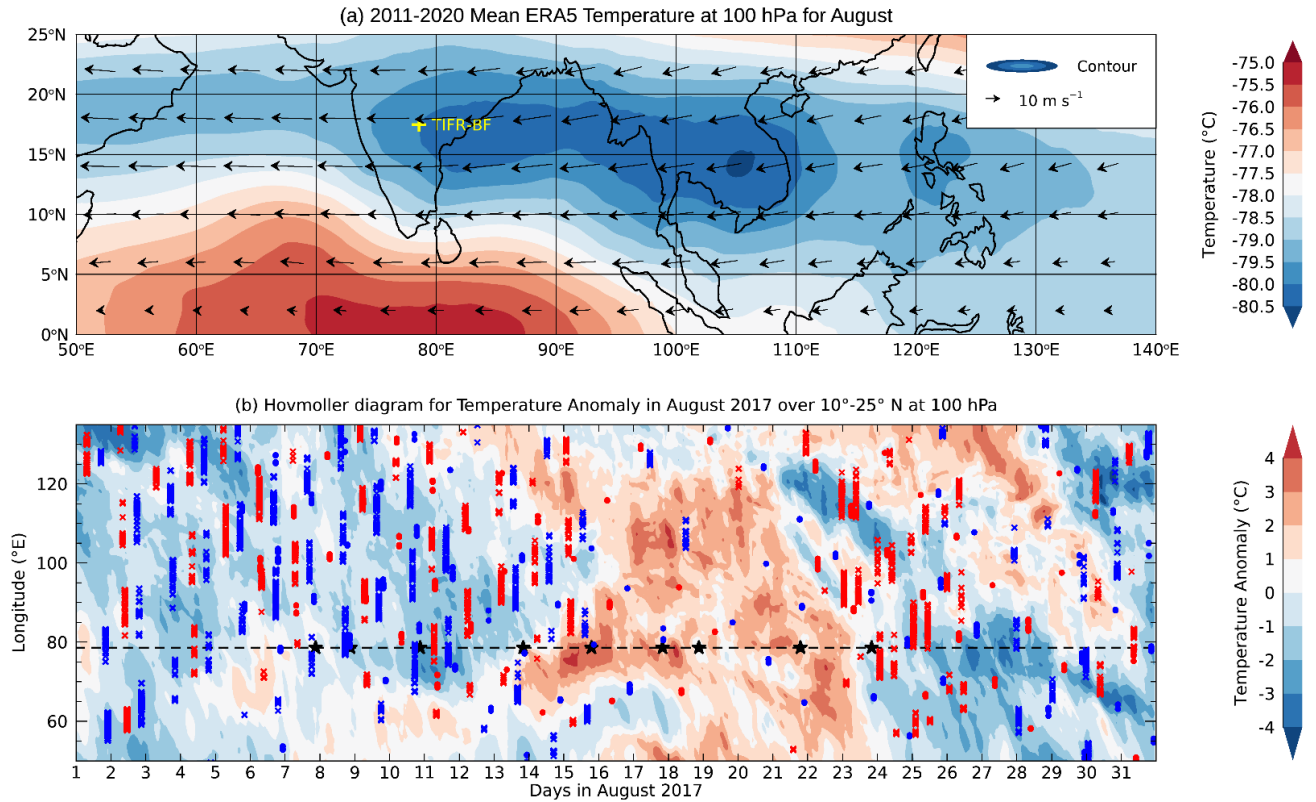
Figure 1: (a) Filled colour contour showing the 10-year (2011-2020) mean ERA5 temperature superimposed with wind vectors representing the mean ERA5 horizontal wind speed and direction at 100 hPa pressure level for the month of August. The yellow "plus" sign indicates the location of the TIFR-BF in Hyderabad, India. (b) Hovmöller plot for the anomaly in temperature from ERA5 temperature at 100 hPa pressure level for August 2017. The anomaly is computed by subtracting the monthly mean (for August 2017) temperature for each grid between 10° N and 25° N. The dashed horizontal black line marks the longitude (78.58° N) of the TIFR-BF with each black star on it showing the launch time of the balloon. The red (blue) filled circles and crosses superimposed on the filled colour contours represent the locations of cirrus cloud layers detected by CALIOP and CATS during daytime (nighttime), respectively, with their base altitude located at 16 km or above.

August), deep convective clouds developing over the Bay of Bengal (BoB) and over the land, especially over the Indian East Coast, cause precipitation in the late afternoon and early evening hours. Climatologically, Hyderabad receives highest rainfall during the months of July and August due to frequent deep convection. Launching a heavy plastic balloon flight from TIFR-BF during this time is thus quite challenging due to strong south-westerly surface winds and frequent precipitation. During this period, the Tropical Easterly Jet (TEJ) with maximum wind speeds of about 40 m s^{-1} prevails over Hyderabad in the UTLS region (Vernier et al., 2018). TEJ brings moisture from the

Bay of Bengal, Western Pacific, and Southeast Asia (Das et al., 2011) necessary for cirrus cloud formation. Also, the tropopause over Hyderabad is extremely cold (minimum temperature reaching about -86°C) as observed during the BATAL campaigns (Vernier et al., 2018) as compared to north India. The 10-year (2011-2020) mean temperature at 100 hPa pressure level (~16.5 km altitude) from ERA5 (described in Sect. 2.4.3) during the month of August shows a pool of cold-region (with temperature between -78 °C and -80 °C) between 10° N and 20° N from the South China Sea to the Indian East Coast with Hyderabad located right at the edge (Fig. 1a). This cold region, often influenced by deep convective activities and the TEJ, seems to be a hot spot for laminar cirrus clouds as evident from the observations of two space-borne lidars (described in Sect. 2.3.1 and 2.3.2) as shown in Fig. 1(b) for the month of August 2017. The occurrence of these cirrus clouds with their base altitude at or above 16 km is associated with negative temperature anomaly estimated from the ERA5 temperature by subtracting the monthly mean temperature from each grid ($0.25° \times 0.25°$) in this cold pool (Fig. 1b). All these factors make TIFR-BF an ideal location for cirrus cloud studies during the ASM. A total of 9 balloon flights were launched from TIFR-BF during August 2017 (Vernier et al., 2018) and the timings of these flights are shown in Fig. 1(b). The balloon-borne instruments used for measuring the cloud properties are described in Sect. 2.2 below.

2.2 Balloon-borne observations

On the night (at 20:03 UTC or 01:33 LT) of 23 August 2017, balloon-borne instruments onboard a Heavy Flight (HF; see Vernier et al. (2018) for description) were launched from TIFR-BF to measure the vertical distribution of aerosols, clouds and meteorological parameters as described in the sub-sections below. Satellite and model data have also been used in this study to support the balloon observations, which are described in the following sub-sections.

2.2.1 Compact Optical Backscatter AerosoL Detector (COBALD)

COBALD is a unique lightweight (about 500 g) balloon-borne backscatter sonde developed at the Institute of Atmospheric and Climate Science, Swiss Federal Institute of Technology (ETH), Zurich. COBALD enables us to detect optically thin layers of aerosols and clouds at high vertical resolution (Brabec et al., 2012; Cirisan et al., 2014; Martínez et al., 2021; Vernier et al., 2015, 2016, 2018; Brunamonti et al., 2018). Additional details on COBALD is presented in Appendix A. COBALD gives backscatter ratio (BSR) at two wavelengths (455 nm and 940 nm) which is an optical analogue for particle mixing ratio. (The ratio of (BSR_{940}-1) at 940 nm to (BSR_{455}-1) at 455 nm, defined as the colour index (CI), gives qualitative information about particle size (Cirisan et al., 2014; Vernier et al., 2015). On substituting the molecular backscatter coefficient at 455 nm and 940 nm wavelengths, CI reduces to

$$CI = 18 \times \left(\frac{\beta_{p940}}{\beta_{p455}}\right) = 18 \times CR \tag{1}$$

where β_{p455} and β_{p940} are particulate backscatter coefficients at 455 nm and 940 nm, respectively and the ratio $\frac{\beta_{p940}}{\beta_{p455}}$ is called the particulate colour ratio (CR). CR value near unity indicates the presence of cloud layer whereas values below 0.7 indicates aerosol presence (Vernier et al., 2015; Brunamonti et al., 2018). Ångström's exponent

estimated from the BSR_{940} and BSR_{455} is used to estimate the backscatter ratio at 532 nm (BSR_{532}) following Vernier et al. (2015). After applying the Field of View (FOV) corrections to COBALD backscatter coefficient as suggested by Brunamonti et al. (2021), an extinction coefficient profile is obtained at 532 nm wavelength by using the BSR_{532} profile and assuming a constant lidar ratio for cirrus clouds following the CALIOP L2 V4 algorithm where initial lidar ratio is a sigmoid function of centroid temperature ± 10 sr (Young et al., 2018). By integrating these extinction coefficients between the base and top altitudes of the cloud layer, optical thickness (τ) of the cloud layer is estimated. The extinction coefficient derived from the COBALD is used for estimating the IWC of the tropopause cirrus cloud layer using a temperature-dependent parametrized relation derived from the aircraft measurements (Heymsfield et al., 2014) as described in the next sub-section (2.2.2).

2.2.2 SOLAIR Boulder Counter and the estimation of cloud microphysical properties
2.2.2.1 SOLAIR Boulder Counter

The Solair Boulder Counter is a medium-weight (~6 kg) portable, forward scattering-based particle counter from Lighthouse Worldwide Solutions, USA (https://www.golighthouse.com/en/airborne-particle-counters/boulder-counter), which uses an extreme life laser diode at 680 nm as a light source. Particles are sampled at a high flow rate of 28.3 Litres per minute (LPM) and are directed to the laser beam. The light scattered at 45° angles from the particles is collected and focused by collection optics onto a photo diode which converts it into electric pulses. The pulse amplitude is a measure of particle size. The number of pulses as a function of pulse height gives particle counts and size information. Particles are counted in six size channels between 5 µm and 100 µm viz., 5, 10, 25, 40, 50 and 100 µm with 50 % counting efficiency at 5 µm size and 100 % at other size bins. The Boulder Counter's ability to measure large particles allows us to infer the distribution of larger air-borne particles such as cloud droplets and ice crystals from a balloon platform. Particle counts in each bin are recorded onboard every 5 seconds which when divided by the instantaneous sample flow gives particle number concentration for that size bin at that time. Boulder Counter measurements were synchronized with COBALD measurements. The flow is controlled and monitored through an external mass-flow controller system. During the flight, the sample flow decreased gradually with decreasing pressure, but it remained above 10 LPM up to 20 km altitude. The entire system was adapted for balloon measurements and enclosed in a foam box to maintain the operating range of conditions during the balloon flight between 10 ℃ and 40 ℃ of temperature. The system was calibrated at the company before the flight and the performance of this system was also tested in a thermo-vacuum chamber prior to the balloon flight. To the best of our knowledge, this system is used for the first time for measuring ice particles in ice clouds from a balloon platform.

2.2.2.2 Estimation of cloud microphysical properties

Only data during the ascent flight are used for estimating the optical and microphysical properties of cirrus clouds. To estimate the microphysical (particle number concentration, effective diameter, and IWC) and the optical properties (extinction coefficient and lidar ratio) from the Boulder Counter data, a log-normal size distribution

function was fit to the cumulative particle number concentration within the cloud layer. A single mode lognormal size distribution function is expressed as

$$\frac{d}{dr}N(r) = N_0 \frac{\exp\left[-\frac{1}{2}\left\{\frac{ln^2\left(\frac{r}{r_m}\right)}{ln^2\sigma}\right\}\right]}{r ln\sigma\sqrt{2\pi}} \tag{2}$$

where N is the number concentration, N_0 is the total particle concentration in the mode, r is the radius, r_m is the median radius, and σ is the width of the distribution (Thomason and Peter, 2006). A previous study (Kuhn and Heymsfield, 2016) has shown that a log-normal distribution provides better match with the data in contrast to a gamma distribution. The first and the third moments of the size distribution are calculated from equation (2) which are then used to estimate the effective diameter (D_e) and IWC, respectively (described below).

The effective diameter of ice crystals is an important microphysical parameter used for the radiative calculations of ice clouds. It is defined as the ratio of absorption to the extinction cross-section of the ice crystals (Foot, 1988). Approximating ice crystals as spheres, D_e can be estimated using a log-normal particle size distribution from equation (3) as shown below:

$$D_e = 2 \cdot \frac{\int_0^r r^3 N(r)dr}{\int_0^r r^2 N(r)dr} \tag{3}$$

where the numerator and the denominator are the third and second moments of the particle size distribution function, respectively. We also estimated the effective diameter using its temperature dependence relation given by Heymsfield et al. (2014) as shown below in equation (4) to compare with that derived from the size distribution.

$$D_e = \alpha e^{\beta T} \tag{4}$$

where T is the temperature,

$\alpha = 308.4$, $\beta = 0.0152$ for -56 °C $< T <$ 0 °C.

$\alpha = 9.1744 \times 10^4$, $\beta = 0.177$ for -71 °C $< T <$ -56°C.

$\alpha = 83.3$, $\beta = 0.0184$ for -85 °C $< T <$ -71°C.

Using the Airborne Tropical TRopopause EXperiment (ATTREX) campaign data, Thornberry et al. (2017) have found that the effective diameter decreases more sharply at temperatures (T) below -81 ℃ (192 K) than previously found by Heymsfield et al. (2014). This decrease in median effective diameter for T<192 K is expressed as

$$D_e = 12 + 28e^{0.625(T-192)} \tag{5}$$

We also estimated the extinction coefficient from our particle size distribution measurements, using a geometric optical approximation which assumes that the extinction coefficient is two times the total cross-sectional area of the ice crystals. Assuming that the ice particles are close to being spherical, we use the equation for extinction expressed in Thornberry et al. (2017):

$$\sigma_{ext} = 2 \times \sum_j N_j \pi r_j^2 \tag{6}$$

where N_j is the ice particle number concentration (in L^{-1}) corresponding to the particle radius r_j (in µm) with j ranging from 1 µm to 25 µm. The ratio of σ_{ext} (from equation 6) to the particulate backscatter coefficient (β_p) obtained from COBALD gives lidar ratio (discussed in Sect. 3.3.4). More details on the lidar ratio are presented in Appendix A.

IWC is an important microphysical parameter for estimating the radiative impact of cirrus clouds as well as for understanding the microphysical and dynamical processes occurring within them (Heymsfield et al., 2017). We estimated IWC for the tropopause cirrus independently from the COBALD backscatter and the Boulder Counter measurements. IWC was obtained from COBALD data using the extinction coefficient (σ_{ext}) and the effective diameter (D_e) estimated from the Equation 9 (e) given in Heymsfield et al. (2014) as shown below.

$$IWC = \sigma_{ext}\left(\frac{0.91}{3}\right)D_e \qquad (7)$$

Here, D_e is obtained from equation (4) using temperature measurements. Using the ATTREX in situ measurements, Thornberry et al. (2017) have given a new parameterization relation for the estimation of IWC from extinction coefficient in the temperature (T) range between 185 K (-88 °C) and 192 K (-81° C) as shown below.

$$IWC = \frac{0.92}{3}\sigma_{ext}\left(12 + 28e^{0.65(T-192)}\right) \qquad (8)$$

IWC is estimated by multiplying the ice-density (917 kg m^{-3}) with the total volume obtained from the third moment of the particle size distribution. IWC for the tropopause cirrus cloud layer derived from these abovementioned methods are compared in Sect. 3.3.5.

2.2.3 India Meteorological Department (IMD) radiosonde profiles from the University of Wyoming

We use daily (00 UTC) radiosonde profiles of meteorological parameters over the Meteorological centre, Hyderabad airport (17.45° N, 78.46° E) and its surrounding IMD stations such as Machilipatnam (16.2° N, 81.15° E), Visakhapatnam (17.7° N, 83.3° E), and Jagdalpur (19.08° N, 82.02° E), obtained from the University of Wyoming Atmospheric Soundings website (http://weather.uwyo.edu/upperair/sounding.html). Only profiles during the month of August 2017 are used in this study from these stations. The monthly mean temperature and wind profiles are constructed by using 27 days of available data over Hyderabad during August 2017. The monthly mean temperature and wind profiles are used to obtain anomalies from the profiles obtained on 23rd August 2017. In order to obtain gravity-wave characteristics, profiles of zonal and meridional wind speed anomalies are used to perform hodograph analysis by following a method described in Leena et al. (2012). The results of hodograph analysis are presented in Section 3.4.3 and in the supplementary information.

2.3 Satellite observations
2.3.1 Cloud Aerosol LIdar with Orthogonal Polarization (CALIOP)

CALIOP was a dual wavelength (532 and 1064 nm), dual-polarization, three channel space-borne lidar onboard the Cloud-Aerosol Lidar and Infrared Pathfinder Satellite Observations (CALIPSO) orbiting around the Earth in a sun-synchronous polar orbit at an altitude of about 705 km and an inclination of about 98.2° (Winker et al., 2009). It

has provided optical properties of aerosols and clouds distributed vertically in the Earth's atmosphere for 17 years since June 2006 at unprecedented spatial resolution with a repeat cycle of 16 days at a given location. CALIOP can detect thin and subvisible cirrus clouds (Martins et al., 2011) by measuring the attenuated backscatter coefficients (at two wavelengths and two polarizations), followed by the retrieval of 532 nm extinction coefficients (Young et al., 2018). IWC and effective diameter are estimated from these retrieved extinction coefficients, using a temperature-dependent empirical fit derived from aircraft data (Heymsfield et al., 2014). In this study, we use CALIOP Level 2 version 4.2 cloud profile (CPro) and cloud layer (CLay) data products having a horizontal resolution of 5 km along the orbit track and 60 m vertical resolution between 8.2 and 20 km altitude range. We obtained scattering ratio profiles from the total backscattering coefficient profiles at 532 nm wavelength and molecular density profiles provided in the CPro data using method described in CALIOP Algorithm Theoretical Basis Document (ATBD, Young et al., 2008).

2.3.2 Cloud-Aerosol Transport System (CATS) lidar

CATS was a three wavelength (355 nm, 532 nm and 1064 nm), dual polarization space-borne lidar intended to provide vertical distribution of aerosols and clouds from the International Space Station (ISS) platform (Yorks et al., 2014). It was launched in January 2015, operated until October 2017, and provided 33 months of aerosol and cloud data. The orbit of ISS has an inclination of 51° and an altitude of about 405 km. This geometry provided more coverage over the tropics and mid-latitudes when compared to CALIPSO with a shorter repeat cycle of 3 days and observations at various local times. In this study, we use 5 km horizontally averaged M7.2 Level 2, Version 3.0 Operational Layer (OL) and Profile (OP) products. These products are obtained from one of the two operational modes (M7.2) of CATS in which backscatter coefficient and depolarization ratio at 1064 nm are measured. The horizontal and vertical resolutions are same as CALIOP data. We obtained scattering ratio from the backscattering coefficient measurements at 1064 nm wavelength and molecular density profiles provided in the data using method provided in CATS ATBD (Yorks et al., 2015).

2.3.3 Cloud top height from Himawari-8 brightness temperature

Himawari-8 is a geostationary satellite launched by Japan Meteorological Agency in October 2014 to observe weather phenomena in 16 spectral bands (visible, near-infrared and infrared) at high resolution (Bessho et al., 2016). Cloud-top temperature observations from 10.4 μm channel of the Himawari-8 satellite at an interval of 10 minutes have been used as proxy for convection. Low cloud-top temperature indicates the presence of deep convective clouds and anvils. The horizontal resolution of cloud-top temperature is ~ 2 km at satellite nadir for the infrared bands. The influence of deep convection on the tropopause cirrus clouds sampled by our balloon is investigated by using a technique combining back-trajectory analysis (described in Sect. 2.4.1) and cloud-top brightness temperature observations at 10.4 μm from the Himawari-8 developed by Bedka and Khlopenkov (2016). This technique has been used earlier in Vernier et al., (2018) for studying the impact of deep convection including overshooting convection on the air parcels sampled by the balloons.

2.3.4 Humidity measurements from Aura-Microwave Limb Sounder (MLS)

Level 2 Version 4.2 relative humidity with respect to ice (RHi) and water vapour mixing ratio (WVMR) data products (Lambert et al., 2015) from the Microwave Limb Sounder (MLS) instrument onboard NASA's Aura satellite are used. These data products are available at 55 pressure levels between 1000 and 10^{-5} hPa. The vertical resolution of MLS-RHi range from 3.7 to 4.6 km between 68 and 100 hPa with an accuracy from 20 to 25 %. The vertical resolution of MLS H_2O product is ~3 km with an accuracy of 8-9 % between 68 and 100 hPa levels. Horizontal resolution along the orbit track is between 190 and 198 km over these pressure levels. The data screening criteria specified for RHi and H_2O data by Livesey et al. (2017) have been applied to filter out the effect of clouds.

2.3.5 Temperature profiles from Global Navigation Satellite System Radio Occultation (GNSS-RO)

High-resolution Global Navigation Satellite System Radio Occultation (GNSS-RO) dry temperature profile product (Level 2, atmPrf) obtained from COSMIC-1, Metop A/B, GRACE, KOMPSAT-5, TSX, and TDX missions are used to find the temperature near the tropopause cirrus clouds detected by CALIOP and CATS. These data are provided by COSMIC Data Analysis and Archive Center (CDAAC, https://cdaac-www.cosmic.ucar.edu/cdaac/products.html) at 100 m altitude grids from 0 to 40 km altitude. Comparison of GNSS-RO temperature profiles with those from radiosonde has shown good agreement (Anthes et al., 2008). GNSS-RO data set have found many applications in the atmospheric science research such as in the study of the gravity waves (Liou et al., 2003), thermal structure of the tropical cyclones (Biondi et al., 2013, 2015; Ravindra Babu et al., 2015), volcanic cloud detection (Biondi et al., 2017), stratospheric thermal perturbation after 2019/2020 Australian pyroCb event (Khaykin et al., 2020) and tropopause cold-anomalies during the 2015 El Nino event over the Pacific ocean (Ravindrababu et al., 2019).

2.4 Model simulations and reanalysis data

2.4.1 NASA Langley Trajectory Model (LaTM) simulations

The influence of deep convection on the tropopause cirrus cloud is investigated by using a combination of back-trajectory analysis and cloud-top temperature observations from the Himawari-8 geostationary satellite (described in Sect. 2.3.3). Meteorological fields from the NASA Global Modelling and Assimilation Office (GMAO) Goddard Earth Observing System, Version 5.2 Forward Processing (GEOS-5.2 FP; Lucchesi et al., 2017) reanalysis are used to compute three-dimensional back-trajectories using the NASA Langley Trajectory Model (Fairlie et al., 2009, 2014). Back-trajectories from the location of the balloon measurement are run at every 100 m vertical resolution. Temperature and wind speeds along the back-trajectories have also been obtained and used in this study to understand the cloud-formation in the air-masses.

2.4.2 NOAA HYSPLIT trajectories

We used National Oceanic and Atmospheric Administration (NOAA) Hybrid Single-Particle Lagrangian Integrated Trajectory (HYSPLIT) model (https://www.ready.noaa.gov/HYSPLIT.php) to compute forward trajectories of the air parcels from the cirrus cloud altitudes measured from our balloon payload.

2.4.3 ERA5 reanalysis data

We use hourly gridded ($0.25° \times 0.25°$) temperature, relative humidity, and wind speed from the ERA5 data product to understand the spatio-temporal variation of the meteorological variables and to supplement the satellite observations. ERA5 is the fifth generation of ECMWF reanalysis data product, which provides improved representations of the troposphere and tropical cyclones at high spatial and temporal resolution than its predecessor ERA-interim (Hersbach et al., 2020). With reference to the high-resolution GNNS-RO temperature profiles, ERA5 temperature data provide most realistic tropopause temperatures compared to other reanalyses (Tegtmeier et al., 2020). We derive the WVMR using the ERA5 temperature and relative humidity data. The ice saturation vapour pressure is obtained from the relation given by Murphy and Koop (2005). Over the ASM region, the WVMR obtained from ERA5 data provide a good representation of its vertical distribution and variation between 60 and 100 hPa pressure levels with an average overestimation by 0.7-0.9 ppmv (15-17 %) compared to that observed by Cryogenic Frost-point Hygrometer (CFH) during the ASM (Brunamonti et al., 2019).

We list different sources of data and key parameters obtained from different instruments as discussed above in Table 1.

Table 1: List of different data sources and key parameters used in this study.

S. No.	Instrument/model/reanalysis data	Key parameters
	Balloon-borne measurements	
1.	COBALD	Backscatter ratios at 455 nm and 940 nm and colour ratio.
2.	iMet-1 radiosonde	Temperature (T), RH, u and v winds, GPS co-ordinates and ascent rate.
3.	Solair Boulder Counter	Particle number concentration at six size channels, D_e, extinction coefficient, and IWC
4.	India Meteorological Department radiosonde profiles	T, RH, u, and v winds
	Satellite Observations	
5.	CALIOP	Cloud base and top height, backscatter ratio, depolarization ratio, colour ratio, D_e, extinction coefficient, and IWC
6.	CATS	Cloud base and top height, backscatter ratio and depolarization ratio
7.	Himawari-8	10.4 µm cloud-top temperature and anvil top height
8.	Aura-MLS	Water vapor mixing ratio and RHi
9.	GNSS-RO	Temperature profiles
	Models/Reanalysis	
10.	NASA LaTM	Back-trajectories
11.	NOAA HYSPLIT	Forward-trajectories
12.	ERA5 reanalysis	T, RH, water vapour mixing ratio, u, and v winds

3 Results and discussion

3.1 Radiosonde, COBALD, and Boulder Counter observations

This section describes the measurements of clouds and background meteorological parameters from the balloon-borne instruments on 23 August 2017. The trajectory of this balloon flight and the temporal variation of the atmospheric conditions measured by the radiosonde are shown respectively in Fig. S1(a) and (b) in the Supplementary Information (SI hereafter). The vertical profiles of BSR_{940}, BSR_{455}, and CR obtained from COBALD during the ascent flight show several peaks (Fig. 2(a)). The peaks in the BSR_{940} profile and the corresponding CR values close to unity clearly indicate the presence of five distinct cloud layers labelled as CL1, CL2, CL3, CL4 and CL5, respectively, in the free troposphere from bottom to top (Fig. 2a). Simultaneous measurements from the Boulder Counter shown in Fig. 2(c) reveal the prominence of particles larger than 5 μm (diameter) in these cloud layers. These particles could be water droplets and/or ice crystals depending on the air temperature which is shown in Fig. 2(b) along with the wind speed. In what follows we describe the characteristics of each of these cloud layers from the lowest to the highest.

Specifically, CL1 is a thin mid-level cloud layer (Bourgeois et al., 2016) with its base located at about 4.1 km near the 0 ℃ isotherm and having a geometrical thickness of about 0.7 km. It is also associated with a shallow temperature inversion present near its centre, which might be responsible for its formation as mentioned by Bourgeois et al. (2016). Since CL1 is located at temperature near the 0 ℃ isotherm we do not expect ice crystals in it. This layer is characterized by a low concentration (less than 10 L^{-1}) of liquid droplets having size smaller than 40 μm with the majority being between 5 and 10 μm in size. CL2 is a geometrically and optically thick (optical thickness at 532 nm ~ 0.37) cloud layer with cloud base and top altitudes at 8.8 km and 11.3 km, respectively. It consists of a high concentration of particles spread over a wide size range. Since this cloud layer lies between the temperature of -27 ℃ and -45 ℃, it could be a mixed-phase cloud layer having both super-cooled water droplets as well as ice crystals (Korolev et al., 2017). However, its cloud top is colder than -40 ℃ indicating the presence of ice crystals which are smaller than 40 μm. These ice crystals have likely grown larger at the expense
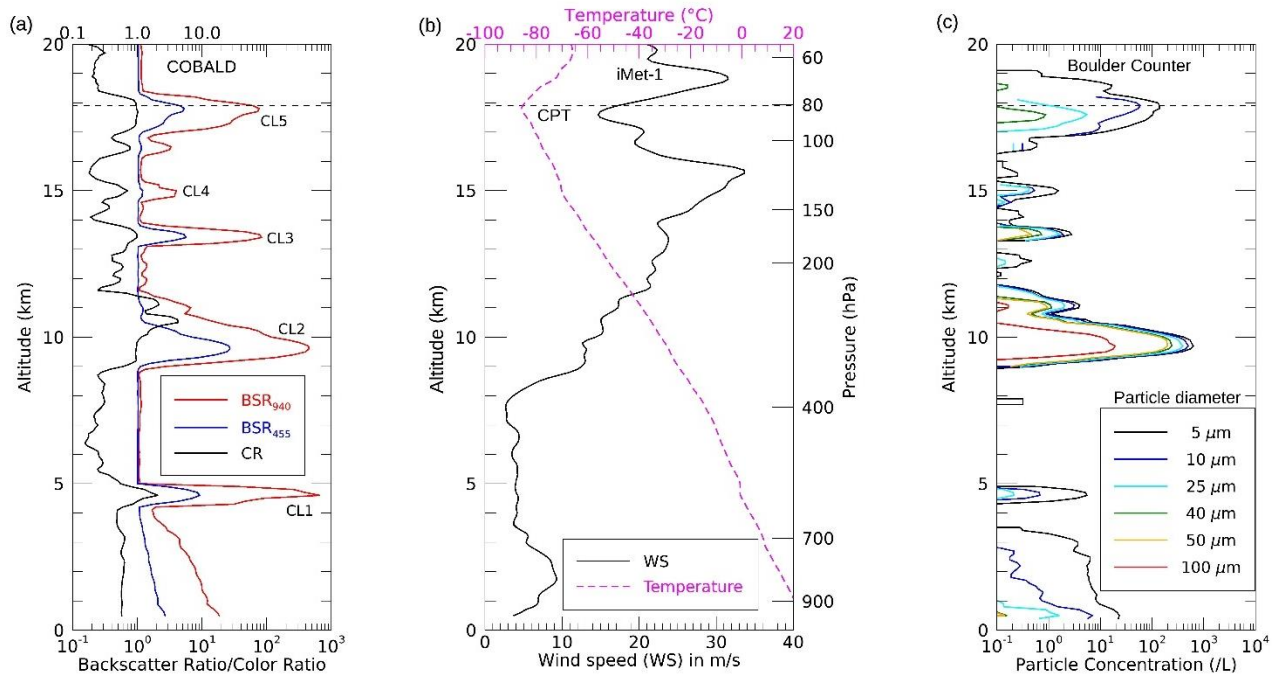
Figure 2: Vertical profile of (a) backscatter ratio at 455 nm (blue line), 940 nm (red line) and colour ratio (black line) obtained from COBALD, (b) temperature (magenta dashed line) and wind speed (black line) from radiosonde with horizontal dashed black line showing the CPT and (c) cumulative particle number concentration for particles having diameter greater than 5 (black line), 10 (blue line), 25 (cyan line), 40 (green line), 50 (yellow line) and 100 μm (red line) obtained from the Boulder Counter measurements on 23 August 2017 over Hyderabad, India during BATAL campaign. The vertical resolution is 100 m for each profile.

of ambient supersaturation and consequently have undergone sedimentation, as evidenced from the increased concentration of larger sized (>40, 50 and 100 μm) ice crystals a few hundred meters below the cloud top and near the cloud base (Fig. 2c). The peak in BSR_{940} almost coincides with the peaks of particle concentration corresponding to each size bins. The peak particle concentration (for diameter > 5 μm) in CL2 is found to be about 732.5 L^{-1} at an altitude of ~9.6 km with the majority of particles sized between 50 and 100 μm and a small number of particles larger than 100 μm. Above this layer, three layers (CL3, CL4 and CL5) of cirrus clouds (as the temperature is below -40 ℃) are observed having low concentrations (less than 10 L^{-1} in CL3 and CL4 and less than 200 L^{-1} in CL5) of ice crystals. In CL3, ice crystals are smaller than 100 μm and in CL4 they are smaller than 40 μm. CL5 is a subvisible (optical thickness at 532 nm of ~ 0.025) cirrus cloud layer located at the CPT. The CPT is located at an altitude of about 17.9 km having a temperature of about -86.4 ℃ (Fig. 2b). CL5 has a geometrical thickness of about 2.1 km with its top located at ~18.3 km in the lower stratosphere, ~ 400 m above the CPT. Note that the peak in BSR_{940} and peaks in particle concentration corresponding to the 5 and 10 μm size bins are located exactly at the CPT. CL5 consists of particles smaller than 50 μm with most of the particles smaller than 25 μm. This tropopause cirrus is again detected by the COBALD during the descent flight between 21:49 UTC and 21:51 UTC at almost similar altitude and similar temperature nearly 100 km southwest from the location of CL5 as shown in Fig. 3(a). About five hours later, a similar tropopause cirrus cloud layer was noticed in the CATS lidar observations as discussed in the next section. In the subsequent sections we discuss the properties of CL5.

      3.2 CATS lidar observations of the tropopause cirrus cloud layer
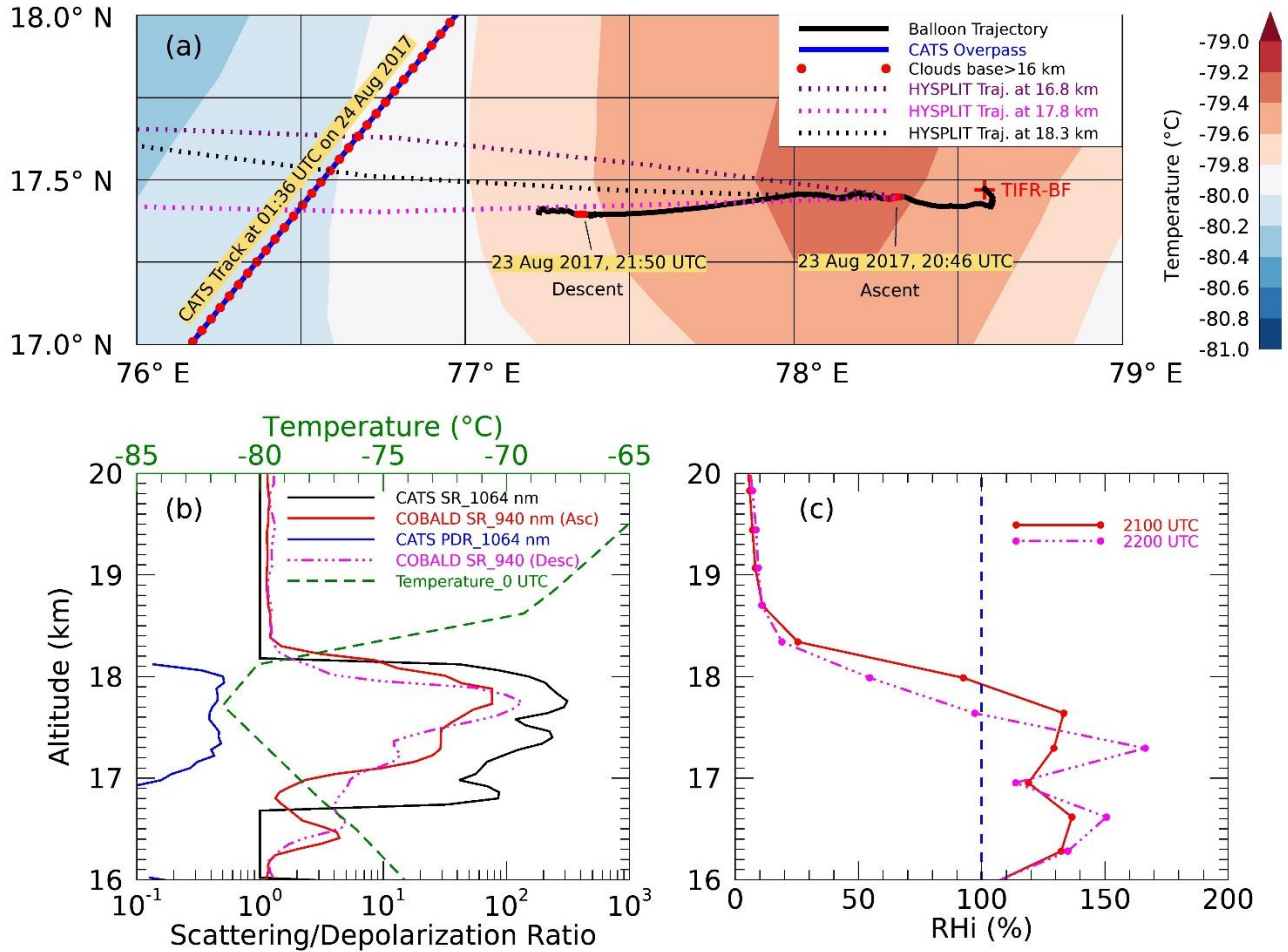
5   **Figure 3: (a) ERA5 temperature at 100 hPa on 24 August 2017 averaged between 01:00 and 02:00 UTC.**
6   **CATS overpass is shown by solid blue line with filled red circles superimposed on it representing the**
7   **locations of cirrus clouds with base height greater than 16 km. Solid black line shows the balloon flight**
8   **trajectory from TIFR-BF on 23 August 2017 (shown by red plus sign) with red circles representing the**
9   **locations of cirrus clouds with base altitude above 16 km during the ascent (at around 20:46 UTC) and**
10 **descent (at around 21:50 UTC). Dashed lines show the forward trajectories from the location of tropopause**
11 **cirrus at 16.8 km (purple), 17.8 km (magenta) and 18.3 km (orange), respectively. (b) Vertical profiles of**
12 **scattering ratio obtained from CATS (at 1020 nm wavelength) and COBALD (at 940 nm wavelength)**
13 **measurements. CATS profiles are averaged between 17.40° N and 17.65° N region along its orbit track. (c)**
14 **Vertical profiles of relative humidity with respect to ice (RHi) from ERA5 during the ascent (2100 UTC) and**
15 **descent (2200 UTC). The vertical dashed blue line marks 100% relative humidity with respect to ice.**

17 On 24 August 2017 at about 01:36 UTC (~5 hours after CL5 detection), there was an overpass of the ISS nearly 100

18 km west from the location of the tropopause cirrus cloud detected during the balloon descent flight and ~200 km

19 from TIFR-BF. This allowed us to corroborate our balloon observations using the onboard operational CATS lidar

data. Linking the data to its larger regional context, Fig. 3(a) shows a colour contour map of mean cloud cover fraction from ERA5 reanalysis data at 100 hPa pressure level (altitude ~16.8 km) pressure level between 01:00 UTC and 02:00 UTC on 24 August 2017. Both balloon (ascent and descent) and CATS measurements of clouds with base altitudes above 16 km at different times and different locations along the wind direction confirm the large horizontal extent of the tropopause cirrus cloud. The horizontal extent of this cloud layer along the CATS orbit track is found to be more than 500 km (Fig. S2).

We further run forward trajectories using HYSPLIT model initialized at three different altitudes within the CL5 to see whether the cirrus cloud layer detected by CATS is influenced by the same air mass or not. These altitudes correspond to the locations in the vicinity of CL5 base altitude (16.8 km), the CPT (17.8 km), and the top altitude (18.3 km) of CL5. These trajectories are intersected by the CATS orbit track between 17.40 ºN and 17.65 ºN after ~2.5 hours of the passage of air-parcels coming from the CL5, indicating their possible influence. The mean vertical profiles of the backscattering ratio and total depolarization ratio at 1064 nm from the CATS lidar averaged between 17.40 ºN and 17.65 ºN along its orbit track are shown in Fig. 3(b) along with the backscattering ratio profiles from COBALD at 940 nm during the ascent and descent. Although these measurements are at different time, locations and wavelengths, a good qualitative agreement can be seen between the two measurements as far as cirrus clouds near the tropopause are concerned. The value of total depolarization ratio at 1064 nm from the CATS lidar lying between 0.4 and 0.5 confirms that this cloud layer consists of non- spherical ice crystals. The CATS cloud phase algorithm also classifies this layer as an ice-cloud layer (Fig. S2). Daily radiosonde observation at 00 UTC from IMD Hyderabad station (17.45 °N, 78.46 °E) just before the ISS overpass on 24 August 2017 revealed that the CPT altitude is about17.7 km (Fig. 3b) while the CPT temperature is found to be coldest (about -81.5 °C) in the last one week. This tropopause cirrus cloud layer is the focus of this manuscript, and we discuss about its microphysical (ice crystal number concentration, effective diameter, and ice water content) and optical properties (extinction coefficient and lidar ratio) derived from our balloon measurements in the following section (Sect. 3.3). We also investigate and discuss the mechanisms responsible for its formation in Sect. 3.4.

3.3 Microphysical and optical properties of the tropopause cirrus cloud

We got only four altitude bins within the CL5 at 100 m resolution where the estimation of microphysical properties using the size distribution is possible. This is because ice crystals were counted only in a few size bins away from the CPT as shown in Fig. 2(c) and particle concentration in at least four size bins are needed for the solution to converge. Assuming spherical ice crystals in CL5, the log-normal size distributions for particle number and volume concentrations at each of these altitude bins are obtained. Figure 4 shows such distributions for the layer mean particle concentration in CL5. From the size distribution, we derive various parameters as discussed below.
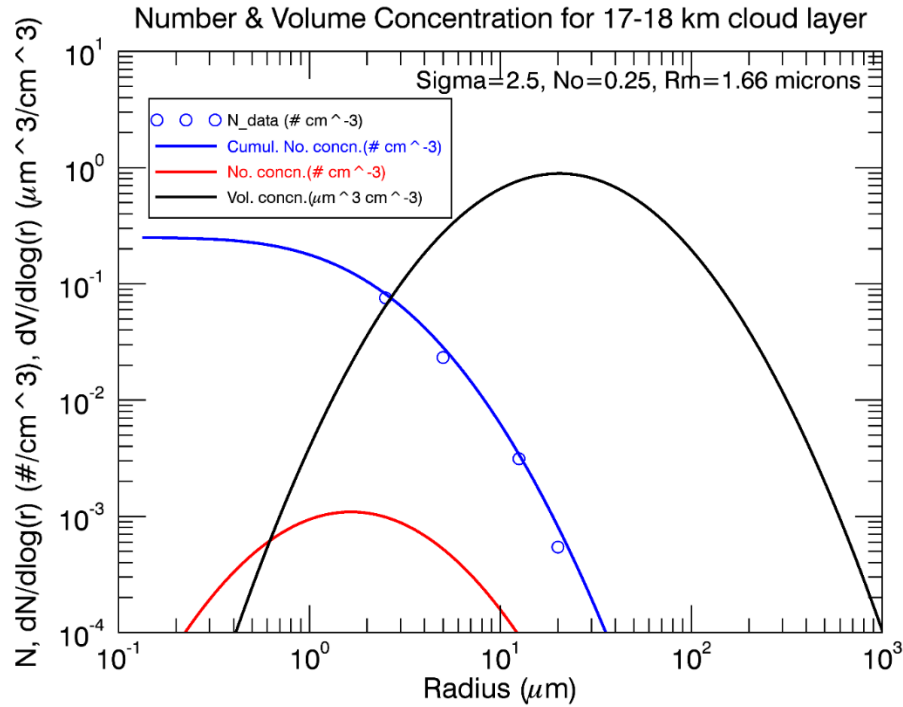
2 **Figure 4: Particle size distribution of the cloud layer (CL5) observed between 17 and 18 km from the Boulder**
3 **Counter measurements on 23 August 2017. Particle number concentration and volume concentration are**
4 **shown by solid red and black lines, respectively. Measured cumulative number concentration is shown by**
5 **open blue circles while the solid blue line is log-normal fit to it. The width of the distribution is given by**
6 **Sigma, which is about 2.5, total particle concentration (N_0) in the mode is 0.25 per cm^{-3} and R_m = 1.66 µm is**
7 **the median radius.**

9 **3.3.1 Ice crystal number concentration (N_{ice})**

10 As shown in Fig. 4, the cumulative ice crystal number concentration for CL5 derived from the log-normal

11 distribution (blue curve) fits well with the measured cumulative number concentration (blue circles). The mean

12 particle number concentration (for diameter > 5 µm) inside the CL5 layer is about 46.79 L^{-1} with a maximum

13 concentration of ~196.3 L^{-1} at the CPT (Fig. 2c). Particle concentration at different altitude bins within CL5 are

14 given in Table 2. These values are in good agreement with those measured inside tropopause cirrus clouds under

15 similar temperatures observed over Bandung, Indonesia (Shibata et al., 2012), the Western Pacific (Woods et al.,

16 2018) and Costa Rica (Lawson et al., 2008).

18 **3.3.2 Effective diameter (D_e)**

20 Using equation (3), the effective diameter (D_e) of ice crystals within CL5 at different altitude bins from 17.3 km to

21 17.7 km are estimated and are shown in Table 2. We have integrated between the radius from 1 to 25 µm because

22 we do not see ice particles larger than 50 µm (diameter) in CL5. D_e varies between 16.34 and 26.61 µm with a

23 mean plus/minus a standard deviation of 20.22±4.54 µm. The mean effective diameter for CL5 between 17.3 and

17.7 km obtained from temperature using equation (4) is about 18.01 ± 0.49 µm while the value obtained using equation (5) (i.e., for temperatures between -81.32 ℃ and -85.76 ℃) is found to be about 21.29 µm. D_e estimated from equation (3) exhibits an increase in its magnitude with decreasing temperature which is contrary to that observed in case of D_e estimated from equations (4) and (5). Increase in D_e estimated from equation (3) is also consistent with increase in particle concentration with gradually increasing contribution coming from larger particles (diameter > 25 µm) near the tropopause as shown in Table 2 and Fig. 2c. The effective diameter for the tropopause cirrus cloud layer observed between 17 and 18 km at temperatures below -83 ℃ by Shibata et al. (2007) was in the range from 8 to 80 µm. Whereas the ATTREX data showed that the median value of D_e reaches near 12 µm at temperatures below -86 ℃ (Thornberry et al., 2017).

3.3.3 Extinction coefficient (σ_{ext})

The values of the extinction coefficients estimated using relation (6) at different altitude bins within CL5 are given in Table 2. The mean and standard deviation of σ_{ext} (0.028 ± 0.009 km^{-1}) are slightly higher than the value 0.018 ± 0.005 km^{-1} obtained from the FOV corrected COBALD backscatter coefficient derived at 532 nm wavelength using a constant lidar ratio of 22 sr. This value of lidar ratio is chosen based on the CALIOP L2 V4 algorithm following Young et al. (2018), where the initial lidar ratio at a cloud centroid temperature (for CL5) of about -81.4 ℃ is about 22 sr. The lower value of the extinction coefficient derived from COBALD could be due to the choice of constant lidar ratio.

3.3.4 Lidar ratio

Table 2 shows the value of lidar ratio inside CL5 at different altitude bins between 17.3 and 17.7 km with a mean and standard deviation of about 32.18 ± 6.73 sr. In this study, the mean lidar ratio is estimated for a mean temperature of ~-83.2 ℃ (see Table 2). To the best of our knowledge, in situ lidar ratio for cirrus cloud at this low temperature has not been estimated before. Our estimates of lidar ratio are in good agreement with those values (40 ± 10 sr) obtained by He et al. (2013) for cirrus clouds observed near the tropopause (temperature ~ -80℃) over the Tibetan Plateau during July and August of 2011. From this study, we demonstrate that the combined measurements from COBALD and Boulder Counter can be used to estimate range-resolved lidar ratio for optically thin cirrus cloud layer near the CPT.

3.3.5 Ice water content

The IWC from the size distribution information provided by the Boulder Counter data is estimated by multiplying the total ice volume by ice density (917 kg m^{-3}). By assuming the spherical shape of the ice crystals, the total volume is estimated from their volume distribution for ice crystal radius ranging between 1 and 25 µm. The values of IWC estimated at different altitude bins between 17.3 and 17.7 km using different methods are shown in Table 2. The mean and standard deviations of IWC estimated from the size distribution between 17.3 and 17.7 km is found to be

about 0.176±0.089 mg/m^3. We also estimated the IWC from the FOV corrected extinction coefficient obtained from COBALD data by using equations (7) and (8) as shown in Table 2. Using equations (7) and (8), the mean and standard deviations of IWC obtained from COBALD data are respectively found to be ~ 0.100 mg m^{-3} and 0.112 mg m^{-3}, which are in good agreement with that obtained from the size distribution data. When considering the entire CL5 layer, mean IWC obtained from COBALD data is found to be about 0.055 mg m^{-3} and 0.062 mg m^{-3} using the relation (7) and (8), respectively. These values are within the range (0.001-10 mg m^{-3}) of the IWC for cirrus clouds observed under similar temperature conditions (-90 °C and -80 °C) during several field campaigns over different regions of the globe (Lawson et al., 2008; Krämer et al., 2016; Heymsfield et al., 2014; Jensen et al., 2017; Woods et al., 2018; Thornberry et al., 2017). The IWC (based on the parametrization relation 7) obtained from the CATS lidar observations between 17 and 18 km altitude, a few hours later of our measurements, is in the range of 0.1-0.6 mg m^{-3}. COBALD and CATS measurements are of the same order, but it is noted that these measurements are at different wavelengths, different sensitivity levels, different times, and locations. Overall, our measurements are within the range of IWC measured for cirrus clouds in similar temperature range over other regions using aircrafts and space-borne lidar. In the next section, we investigate the formation mechanisms of CL5.

Table 2: Optical and microphysical properties of CL5 derived using COBALD and Boulder Counter measurements on 23 August 2017 from TIFR-BF. Data in *italic* fonts show the properties derived using only Boulder Counter data while data shown in normal fonts are derived from COBALD and/or iMet-1 radiosonde data.

Altitude (km)	17.3	17.4	17.5	17.6	17.7	Mean ± Std. dev.
Temperature (°C)	-81.32	-82.26	-83.23	-84.10	-84.94	-83.17±1.43
No. concentration (#/L)	*54.23*	*67.27*	*99.47*	*101.77*	*108.87*	*85.32±25.12*
D_e (μm) using Eqn. 3	*16.34*	*-*	*17.81*	*20.11*	*26.61*	*20.22±4.54*
D_e (μm) using Eqn. 4	18.62	18.36	18.0	17.68	17.41	18.01±0.49
D_e (μm) using Eqn. 5	33.33	25.14	18.56	15.42	14.0	21.29±7.98
σ_{ext} (km^{-1}) from COBALD	0.013	0.018	0.017	0.018	0.026	0.018±0.005
σ_{ext} (km^{-1}) using Eqn. 6	*0.014*	*-*	*0.029*	*0.032*	*0.035*	*0.028±0.009*
β_{p532} (x 10^{-4} km^{-1}sr^{-1})	5.77	8.13	7.71	8.33	12.06	8.40±2.28
Lidar ratio (sr)	24.17	-	37.44	38.04	29.05	32.18±6.73
IWC (mg m^{-3}) using Eqn. 7	0.072	0.099	0.093	0.098	0.140	0.100±0.025

IWC (mg m^{-3}) using Eqn. 8	0.130	0.137	0.096	0.087	0.114	0.112±0.021
IWC (mg m^{-3}) from the size distribution	*0.070*	*-*	*0.157*	*0.195*	*0.285*	*0.176±0.089*

3.4 Investigation of the mechanisms involved in the formation of the tropopause cirrus
3.4.1 Back-trajectories and their intersection with deep convective clouds observed from Himawari-8

Overshooting convection can directly inject ice crystals into the lowermost stratosphere region (Corti et al., 2008; Khaykin et al., 2009; Dessler et al., 2016; Smith et al., 2017; Lee et al., 2019; Khaykin et al., 2022). Under the subsaturated conditions of the stratosphere, these ice crystals subsequently undergo sedimentation and sublimation leading to a hydration patch (Jensen et al., 2020; Lee et al., 2019). This hydration patch could get advected and further lead to secondary ice formation upon cooling near the CPT region. Extreme convective clouds (cloud top heights exceeding 17 km) can also induce cooling near the tropopause (Kim et al., 2018) which eventually could cause dehydration through ice formation. In addition to this, rapid tropopause cooling can also be caused by the convectively induced gravity waves (Kim and Alexander, 2015; Kim et al., 2016) followed by supersaturation, cloud formation and dehydration (Dzambo et al., 2019; Schoeberl et al., 2015, 2016). A recent study (Dzambo et al., 2019) over Australia has shown that the magnitude of tropopause cooling is greater during the monsoon period than that during the non-monsoon periods. CL5 could possibly be a result of the direct injection of ice crystals due to overshooting convection or through cooling caused by one of these processes mentioned above.
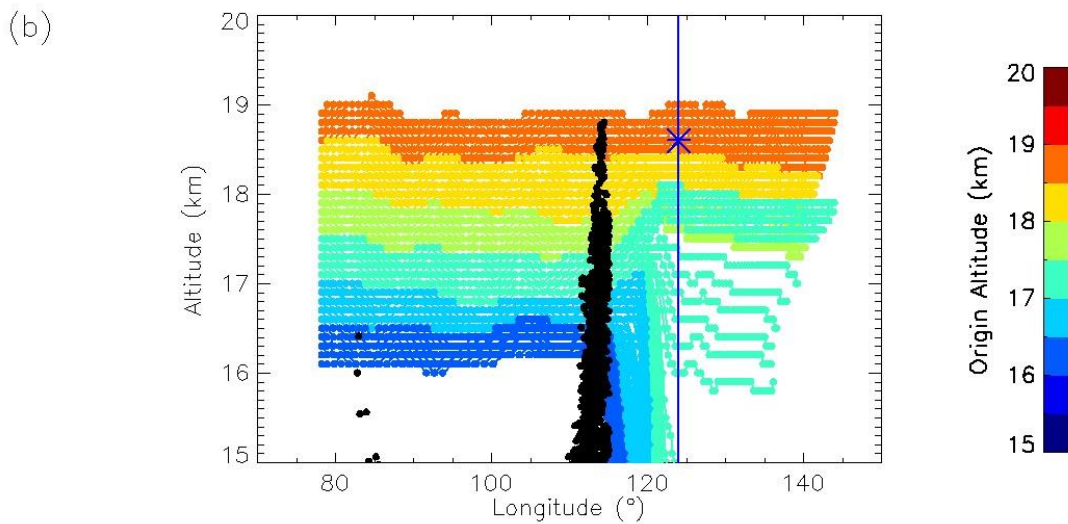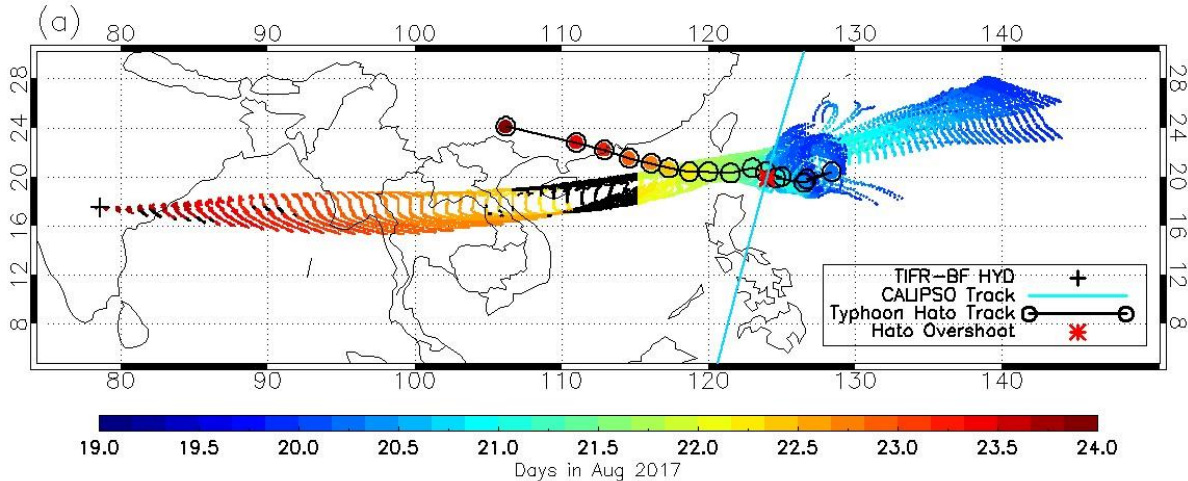
Figure 5: (a) Five-day back-trajectories initialized on 23 August 2017 at 20:00 UTC from the balloon measurement locations at different altitudes between 16 and 19 km represented by coloured dots as a function of latitude and longitude with colour showing the days in August 2017. The locations of deep convective anvil tops observed after 21 August 2017 from the Himawari-8 brightness temperature images at 10.4 μm wavelength channel that intersected the back-trajectories are shown by black dots. Typhoon *Hato* track is shown by black outlined coloured circles connected by black line with colour showing the day fraction. The night-time CALIPSO orbit track on 20 August 2017 between 17:27 and 17:40 UTC is shown by cyan line with the location of the overshooting cloud top shown by red asterisk. (b) Five day back-trajectories represented as a function of longitude and altitude with colour showing their origin altitude. The locations of the anvil top altitude that intersected with the back-trajectories are represented by black dots. The locations of CALIPSO overpass and the overshooting cloud top altitude are shown by blue vertical line and blue asterisk, respectively.

15   The influence of deep convection on the CL5 is investigated by using a combination of back-trajectory

16   analysis and cloud-top brightness temperature observations at 10.4 μm from the Himawari-8 geostationary satellite

17   data as discussed in Sect. 2.3.3. Figure 5(a) shows five-day back-trajectories initialized from the balloon

18   measurement sites between 16 and 19 km as a function of latitude, longitude, and time. The locations of the

convective anvil tops that intersected these air parcels are also superimposed along the back-trajectories. Few isolated localized convective clouds over the Indian East Coast along the back-trajectories can be noticed in Fig. 5(a). While intersecting with the back-trajectories, the anvil top of these convective events does not reach 18 km altitude. But comparisons of GOES-16 (nearly identical to Himawari-8) and Visible Infrared Imaging Radiometer Suite (VIIRS) temperature (Khlopenkov et al., 2021) show that pixel resolution has a strong impact on observed temperatures within convection. Therefore, the highest overshooting tops likely exceeded 18 km height. The convective clouds near the Indian East Coast were also observed by the India Meteorological Department Doppler Weather Radars located at Machilipatnam (16.12° N, 81.09° E) after 12:00 UTC on 23 August 2017 with maximum echo altitude reaching about 17 km (Fig. S3). These convective clouds were at their peak altitudes at around 11:40 UTC as seen in the Himawari-8 images, and we do not have radar images prior to 12:00 UTC or co-located CATS/CALIOP observations to confirm this. However, the intersection of air parcels with these convective clouds over the Indian East Coast took place nearly 6 hours later at around 16:00 UTC during which their anvil top altitude reduced. Based on the Himawari-8 images and back-trajectories, the direct injection of ice crystals by these local convective clouds up to 18 km altitude along the Indian East Coast seems likely. Thus, we cannot fully rule out the influence of local convection because we notice enhanced WVMR at 70 hPa pressure level on 23 August 2017 at 12:00 UTC over the surrounding regions of Hyderabad and the east Coast (see Fig. S3). This enhanced water vapour might be associated with these convective clouds as far as the recent studies on the convective hydration are concerned (Jensen et al., 2020; Ueyama et al., 2018). Enhanced water vapour might have led to the secondary ice formation after undergoing through cold tropopause conditions while subsequent advection towards Hyderabad by the TEJ. Ueyama et al. (2018) showed that the deep convective clouds occurring above 380 K potential temperature level (~17 km) increase in situ formed cirrus clouds by 38 % compared to 21 % by the convective clouds in the range 375-380 K. This could be the case for CL5.

In addition to the hydration, these convective clouds could have also caused cooling near the CPT as discussed by Kim et al. (2018), which could have facilitated the in situ formation of ice crystals. Temperature measurements on 23 August 2017 at different times in and around 400 km radius of TIFR-BF suggest that such cooling has most likely taken place before the arrival of the air parcels as shown in Table 3. Lack of accurate RHi and ice measurements near the CPT over these convective clouds preclude us from confirming in situ formation. Thus, the role of local deep convective clouds in the formation of CL5 is not quite clear due to the lack of observations. High-resolution model simulations of these convective clouds could help in ascertaining their role in the formation of tropopause cirrus clouds, which is beyond the scope of this study.

1 **Table 3: Variation of the CPT temperature and altitude as measured by radiosondes and GNSS-RO in and**
2 **around Hyderabad during 23 and 24 August 2017.**

Date/Time	23 Aug 2017, 00 UTC (Radiosonde)	23 Aug 2017, ~14:00 UTC (GNSS-RO)	23 Aug 2017, 20:55 UTC (Radiosonde)	23 Aug 2017, 21:50 UTC (Radiosonde)	24 Aug 2017, 00 UTC (Radiosonde)
Location	17.45° N, 78.46° E	18.45° N, 81.40° E	17.44° N, 78.30° E	17.40° N, 77.36° E	17.45° N, 78.46° E
Distance from TIFR-BF (km)	13.5	332	38.9	135.5	13.5
CPT altitude (km)	17.20	17.30	17.9	17.75	17.7
CPT temperature (°C)	-77.2	-82.5	-86.4	-86.1	-81.5

5 In Fig. 5(a), we note that the air parcels have already been influenced by deep convective clouds over the South
6 China Sea before their intersection with local convective clouds over the Indian East Coast. The altitude distribution
7 of the back-trajectories shown in Fig. 5(b) suggests that the air parcels initialized from the balloon measurement
8 altitudes between 16 and 18 km have originated from the lower levels (below 10 km) in the region between 115° E
9 and 125° E on 22 August 2017. This large-scale upward movement of the air parcels indicates a synoptic scale
10 convective system, such as a tropical cyclone or a typhoon. Himawari-8 brightness temperature image on 22 August
11 2017 at 19:00 UTC in Fig. 6 does reveal such synoptic scale system named typhoon *Hato,* a category-3 tropical
12 cyclone in the South China Sea, which severely affected the coastal cities of Macau, Zhuhai, and Hong Kong in
13 southern China on 23 August 2017 after its landfall (Li et al., 2018). Typhoon *Hato* intensified to a category-3
14 typhoon just before its landfall (Pun et al., 2019) and it was one of the strongest typhoons in the last several decades,
15 which caused widespread flooding in the Pearl River Delta region in southern China, Macau being the hardest hit
16 city (ESCAP/WMO Typhoon Committee, 2017). The anvil cloud top altitude derived from the Himawari-8 cloud-
17 top temperature images along the back-trajectories are found above 18.5 km (Fig. 5b) with the highest cloud top
18 altitude of about 18.8 km observed on 22 August 2017 at 09:10 UTC over 18.85° N, 114.48° E. It appears that
19 typhoon *Hato* had most likely injected ice crystals in the lower stratosphere as the CPT altitude observed from the
20 nearest radiosonde temperature profile over Haikou station (20.03° N, 110.35° E) at 12:00 UTC was about 17.4 km
21 (Fig. S4). Moreover, the tropopause temperature and tropopause altitude might be substantially reduced by the
22 overshooting convection as pointed out by Sun et al. (2021).
23
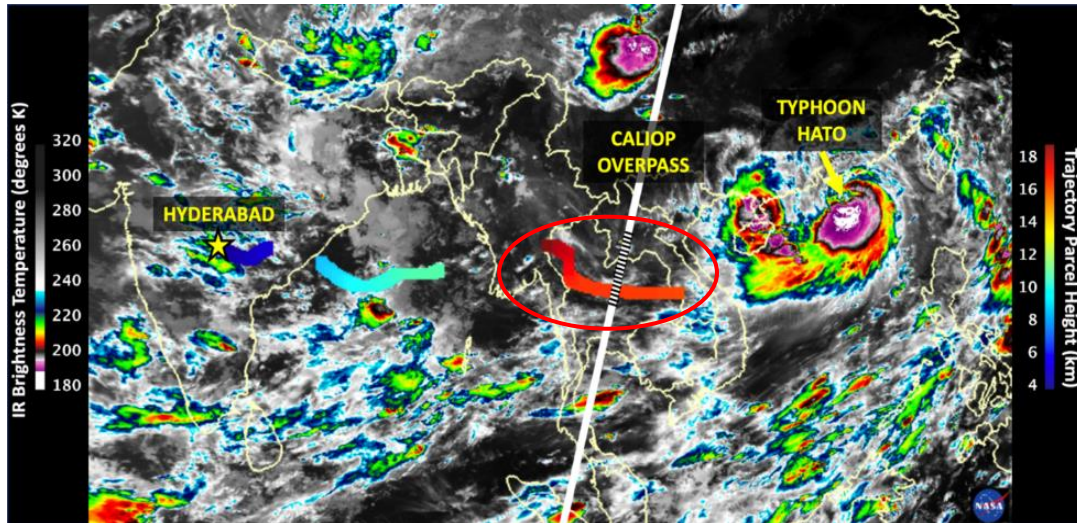
Figure 6: Image of brightness temperature (in Kelvin) at 10.4 μm infra-red channel of Himawari-8 satellite valid for 22 August 2017 at 19:00 UTC over East Asia. Typhoon *Hato* is associated with very low brightness temperature. The altitudes (in km) of back-trajectory air-masses initialized from the balloon measurement site (Hyderabad, India; denoted as yellow star) are superimposed on the image and are represented by thick coloured curves. The air-mass back-trajectories initialized between 16 and 18 km altitude above Hyderabad at the time of the balloon flight on 23 August 2017 are encircled red. The thick white line shows the night-time CALIPSO overpass from 19:06 to 19:20 UTC on 22 August 2017 with black stripes showing the region where tropopause cirrus was sampled.

Ice crystals injected by typhoon *Hato* in the subsaturated lower stratosphere might have caused a hydration patch after undergoing through sedimentation and sublimation while being advected westward by the prevailing easterly winds. The ERA5 WVMR at 70 hPa pressure level on 22 August 2017 at 09:00 UTC indeed reveals such hydration patch (see Fig. S4). We did not have collocated CATS/CALIOP observations at that time to verify this overshooting event. However, there was a nighttime CALIPSO overpass on 20 August 2017 through the developing typhoon between 17:28 UTC and 17:40 UTC (a few hours before the passage of the air parcels) that observed cloud top altitude of about 18.6 km (see Fig. 5a, 5b and Fig. S5). Daytime and co-located night-time profiles of the WVMR from the MLS instrument confirm the presence of such hydration over typhoon *Hato* with peak WVMR reaching ~6.5 ppmv at 82.5 hPa pressure level near the tropopause (Fig. 7b). The location of the clouds observed by CALIOP is well above the CPT observed from the nearest GNSS-RO temperature profile at 22:44 UTC as shown in Fig. 7c. This WVMR value could be even higher after *Hato* intensified to a category-3 typhoon because intensification is followed by frequent long-lasting intense convective bursts(Horinouchi et al., 2020) that increase the possibility of overshooting and direct hydration in the lower stratosphere (Romps and Kuang, 2009; Jiang et al., 2020). Aircraft observations over the Western Pacific region during the NASA's POSIDON campaign have provided evidence for such direct hydration in the outskirts of typhoon *Haima* on 15 October 2016 (Jensen et al., 2020). They observed a layer (~1 km thick) of enhanced water vapour in the lower stratosphere with a peak WVMR of about 7 ppmv at an altitude of ~17.5 km, which could not be resolved by MLS owing to its coarse vertical resolution (see Fig. 2 of Jensen et al. (2020)).
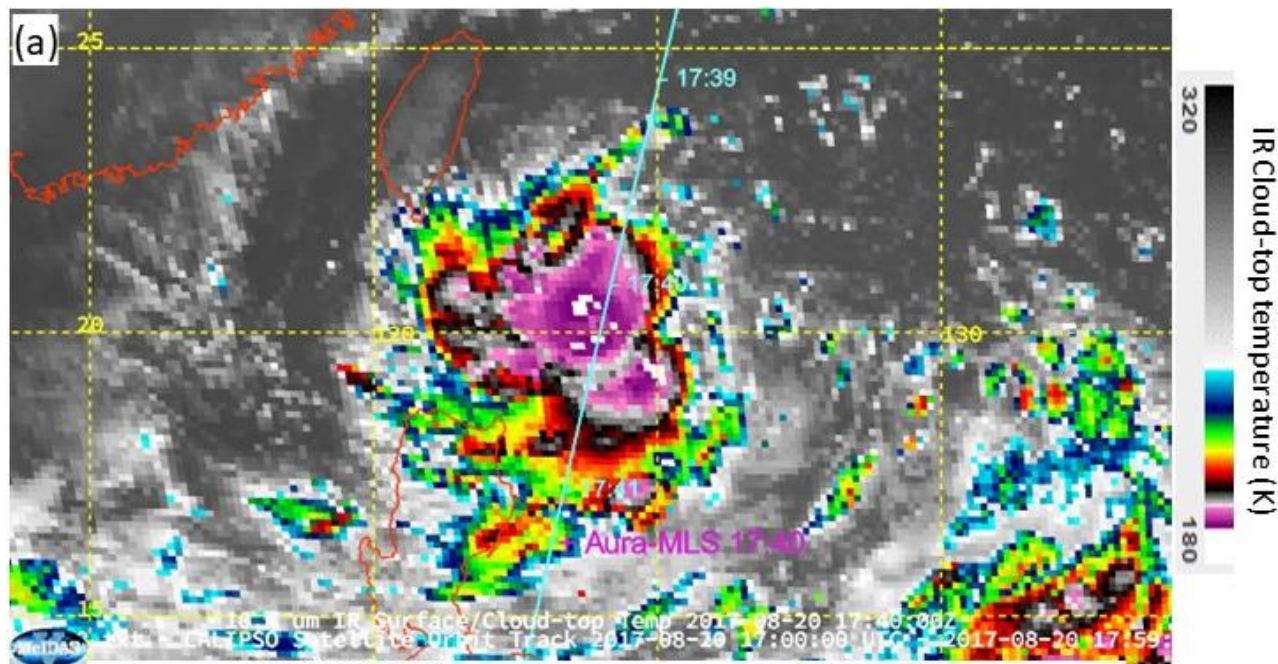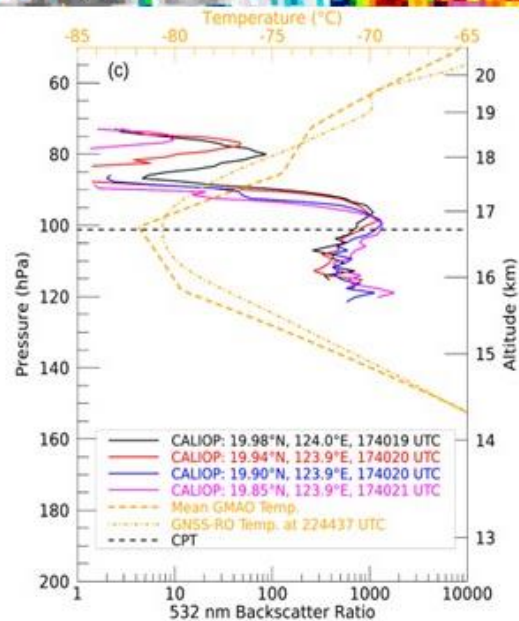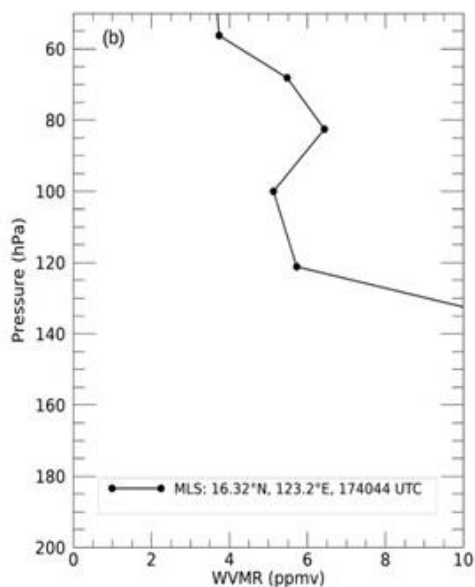
2   **Figure 7: (a) 10.4 μm infrared cloud-top temperature from Himawari-8 at 17:40 UTC on 20 August 2017**
3   **showing the overshoots during the development phase of typhoon *Hato*. The cyan line represents the**
4   **CALIPSO orbit track that observed the overshoot on 20 August 2017 between 17:40 and 17:41 UTC while the**
5   **magenta plus symbol denotes the location of Aura-MLS profile at 17:40 UTC. (b) Vertical profile of water**
6   **vapour mixing ratio (WVMR) from MLS on 20 August 2017 at 17:40 UTC near the overshoot region**
7   **observed during the night-time overpass of Aura satellite. (c) Vertical profiles of 532 nm backscatter ratio**
8   **obtained from the CALIOP on 20 August 2017 at around 17:40 UTC. Dashed orange lines show the mean**
9   **temperature profile obtained from GMAO along the CALIPSO track and from GNSS-RO at 22:44 UTC.**
10   **Dashed horizontal black line represents the CPT.**

Jiang et al. (2020) have studied the impact of 30 tropical cyclones (TC, many of them observed during the ASM) on the UTLS water vapour over the tropical northwestern Pacific Ocean using MLS and CloudSat observations during 2012-2016. They found that the lower-stratospheric water vapour over the TC area increased by an average value of 0.75 ppmv compared to the non-TC area, indicating direct hydration. It seems that the hydration caused by typhoon *Hato* has followed the anticyclonic flow and may have influenced the formation of CL5. We investigate this advection with further water vapour observations from MLS and ERA5 derived WVMR in the next sub-section.

3.4.2 Advection of injected ice and hydration caused by typhoon *Hato*

As discussed in the previous section, the trajectories and the Himawari-8 cloud-top images suggest that the ice crystals detected by our balloon measurements are likely influenced by the convective outflow of typhoon *Hato*, which could possibly be advected to the measurement site by the Tropical Easterly Jet (TEJ) or formed in situ from the moist air-mass (from sublimated overshoot) brought by TEJ near the cold tropopause. We discuss these aspects in this section. TEJ is known to play a significant role in the redistribution of upper-tropospheric moisture and the formation of cirrus clouds during the ASM (Das et al., 2011). However, it can be questioned that the ice crystals sampled by our balloon measurements can survive that long distance (about 4000 km) if they were advected from the outflow of a typhoon because larger particles would eventually sediment and sublimate in a subsaturated region. Assuming the ice crystals to be spheroids (aspect ratio=1), the terminal velocity calculated by using the relationship given by Heymsfield and Westbrook (2010) suggests that both 5 and 10 µm particles will fall less than 1 km in two days. Thus, they are expected to survive within the layer if they were advected from the outflow of typhoon *Hato* by the TEJ provided they do not grow, or sublimate and the background conditions remain the same. These theoretical calculations are consistent with the Boulder Counter measurements which show the dominance of ice crystals smaller than 25 µm in CL5 (Fig. 2c). The presence of ice crystals larger than 10 µm in the middle of the CL5 could be explained by the constant growth, aggregation, and consequent sedimentation within the layer in the outflow.
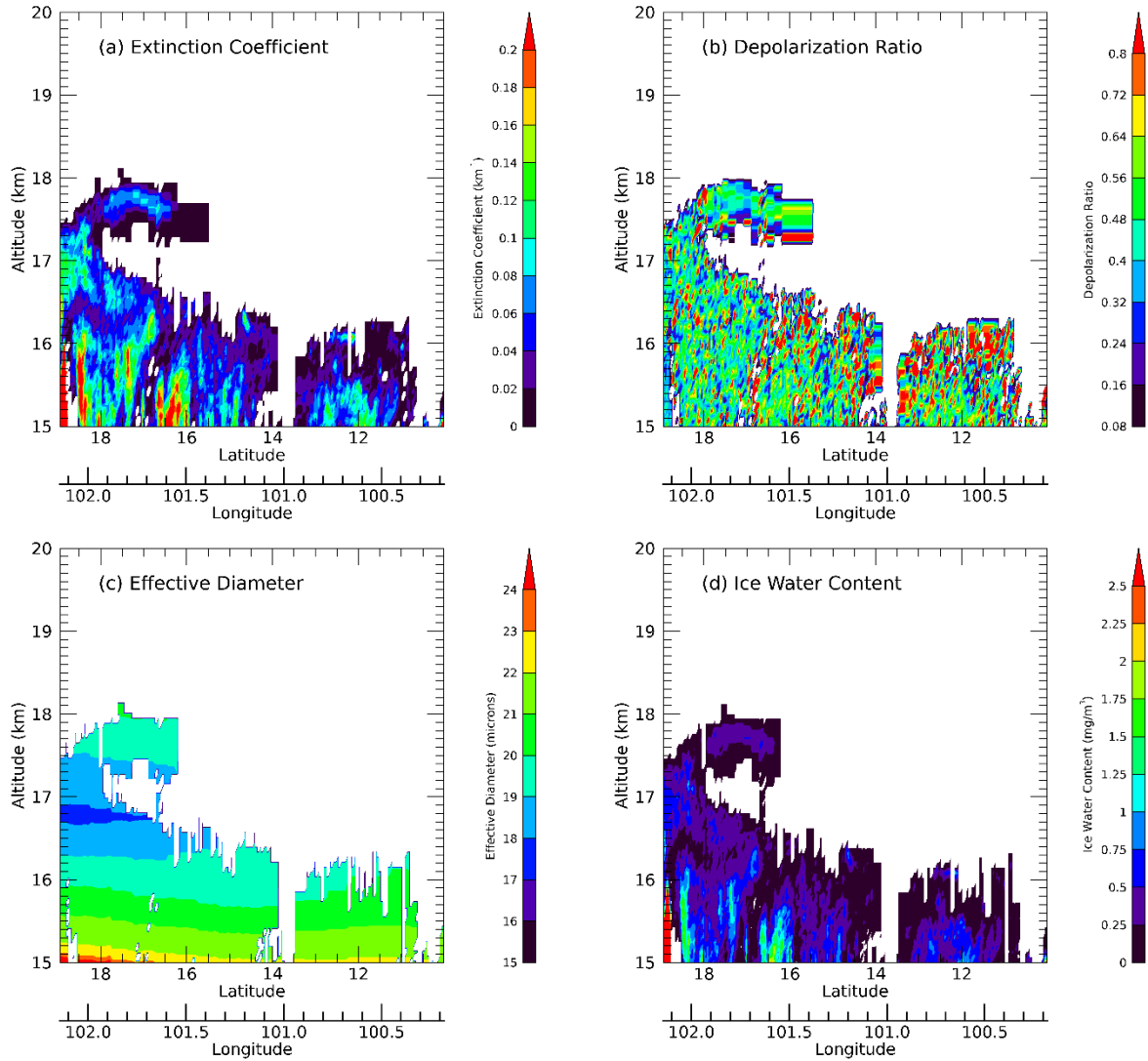
Figure 8: Optical and microphysical properties of cirrus clouds observed by CALIOP on 22 August 2017 at 19:00 UTC over Southeast Asia represented by black stripes in Fig. 6.

A thin cirrus cloud layer can be seen near the tropopause between 17 and 18 km over Laos and Thailand in the night-time observations from CALIOP on 22 August 2017 at around 19:00 UTC along the air parcels coming from the typhoon with properties like CL5 (Fig. 8a-d). This cirrus cloud layer extended horizontally to more than 200 km along the CALIPSO orbit track in the same latitude band (17° N - 18° N) where the balloon measurements were taken. The values of depolarization ratio between 0.3 and 0.6 and colour ratio close to 1 (Fig. S6) in this layer confirm the presence of non-spherical ice crystals. The CALIOP IWC to extinction coefficient ratio provides an estimated effective diameter ranging between 18 and 20 μm, which is consistent with our balloon measurements (20.22 ± 4.54 μm). The peak extinction coefficient value lies between 0.08 and 0.1 km^{-1} and is in the altitude range of 17.6-17.9 km, consistent with the extinction coefficient maxima (0.06 km^{-1} at 17.9 km from COBALD) for CL5. The IWC estimated by CALIOP for this layer using an empirical parametrization developed from aircraft data (Heymsfield et al., 2014) ranges between 0 and 0.5 mg m^{-3}. These similarities in optical and microphysical properties

suggest that the two layers detected by balloon and CALIOP could possibly be formed by the same mechanism under similar background conditions. However, the lifetime of ice crystals in cirrus clouds depend on several local background factors such as temperature, relative humidity with respect to ice, horizontal wind and updraft speed, and the type and quantity of ice-nuclei. These factors may vary rapidly especially in the TTL under the influence of deep convective clouds, TEJ, gravity waves, and relatively high aerosol concentration during the ASM, which could influence the ice microphysics. This means that the ice crystals formed at one location through one mechanism may sublimate and/or crystalize at other locations while moist air is being transported to another location depending upon the local background conditions which force its distribution between ice and gas phases. It is therefore important to keep a track record of these parameters along the back-trajectories. We discuss the role of background conditions such as temperature, water vapour and vertical wind speed on the in situ formation of tropopause cirrus clouds along the back-trajectories in the next sub-section.

As mentioned earlier, the convectively injected ice by typhoon *Hato* in the subsaturated lower stratosphere may undergo sedimentation and sublimation leading to a hydration patch in the lower stratosphere (Lee et al., 2019). To investigate this, we derive WVMR from ERA5 relative humidity and temperature hourly data at 70 hPa over typhoon *Hato* on 22 August 2017 at 09:00 UTC where the peak overshoot was observed from the combined analysis of Himawari-8 and the back-trajectories (Fig. 9a). We see an enhancement in the WVMR located between 15°-20° N and 107°-114° E. As we move forward in time, this enhanced moist plume is seen to be advected towards the west. However, a weaker enhancement in WVMR can also be seen over the Indian East Coast surrounding Hyderabad, probably due to afternoon deep convective clouds, which likely have also assisted the formation of CL5. The advection of moist plume can also be seen in the averaged WVMR at 70 hPa level for 22 and 23 August 2017 with high WVMR between 15° N and 20° N latitudes as shown in Fig. 9(b).
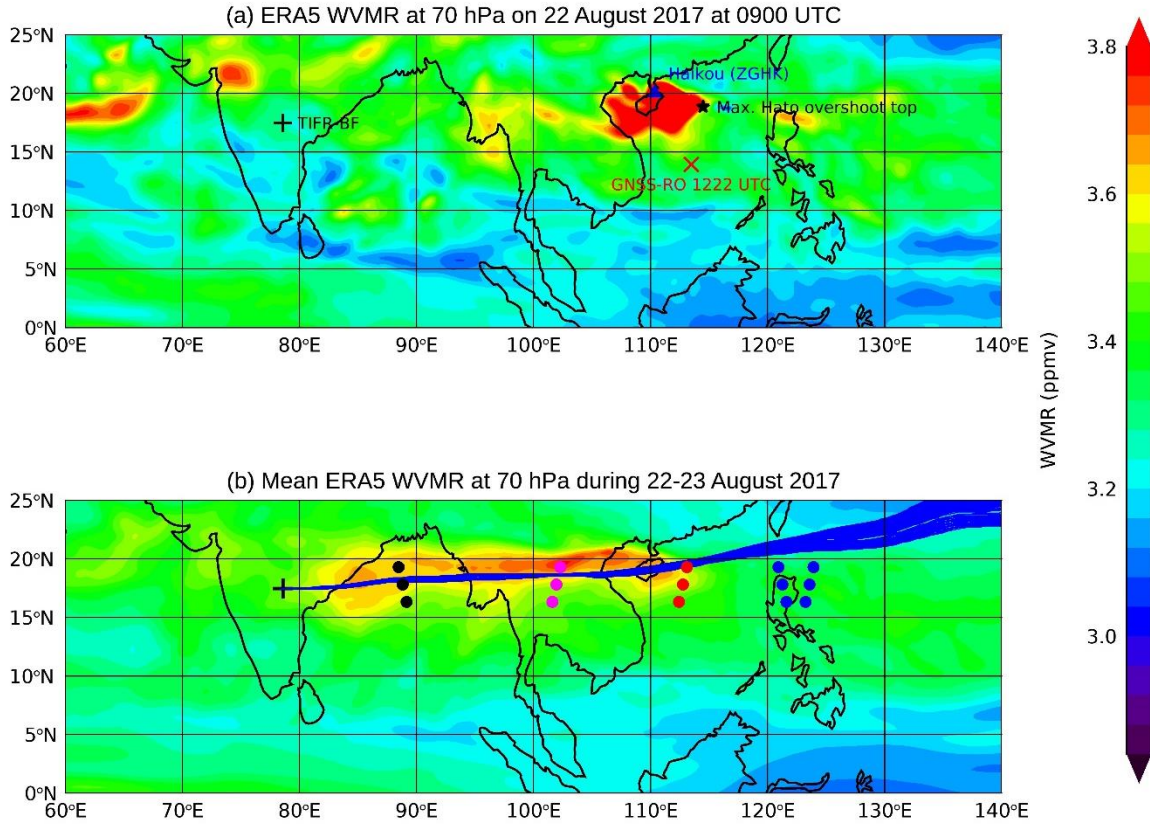
Figure 9: (a) Spatial map of water vapour mixing ratio (WVMR) derived from ERA5 data at 70 hPa level on 22 August 2017 at 09:00 UTC showing large enhancement over the South China Sea. The locations of TIFR-Balloon Facility, Haikou radio sounding station, maximum overshoot top altitude and GNSS-RO profile obtained at 1222 UTC are represented by black plus, blue triangle, black star, and red cross symbols, respectively. (b) Average water vapour mixing ratio derived from ERA5 for 22 and 23 August 2017 at 70 hPa with back-trajectories initialized between 18 and 19 km (between 79 and 68 hPa) from the balloon site represented by blue lines superimposed on it. Nearest MLS footprints with respect to the back-trajectories between 16° and 20° N on 20, 21, 22 and 23 August 2017 are represented by blue, red, magenta, and black filled circles, respectively.

To quantify the transport of this enhanced moisture relative to the monthly mean WVMR at 70 hPa and non-TC area, we estimated WVMR anomaly for the month of August 2017 by subtracting the mean WVMR for each grid over this region (between 15° N and 20° N). The Hovmöller plot in Fig. 10 (a) clearly shows the transport of enhanced moisture (0.6-0.9 ppmv) relative to the monthly mean and reaching Hyderabad on 23-24 August night. We also notice that the magnitude of this enhanced moisture is in good agreement with the results found by Jiang et al. (2020) using MLS observations. We also verified this transport with the MLS WVMR observations during 20 and 23 August 2017 over this region (between 15° N and 20° N) that transacted the back-trajectories nearest in space and time (Fig. 10b). We clearly see enhanced moisture (greater than the monthly mean value) at 82.5 hPa and 68 hPa pressure levels whose magnitude decreases as we move forward in time (from Fig. 10e to 10b). While being advected, this moist plume may get transported downward towards the CPT and may lead to in situ secondary ice

1 formation upon cooling. We present the evidence for such downward transport and cooling near the tropopause

2 along the back-trajectories in section below.
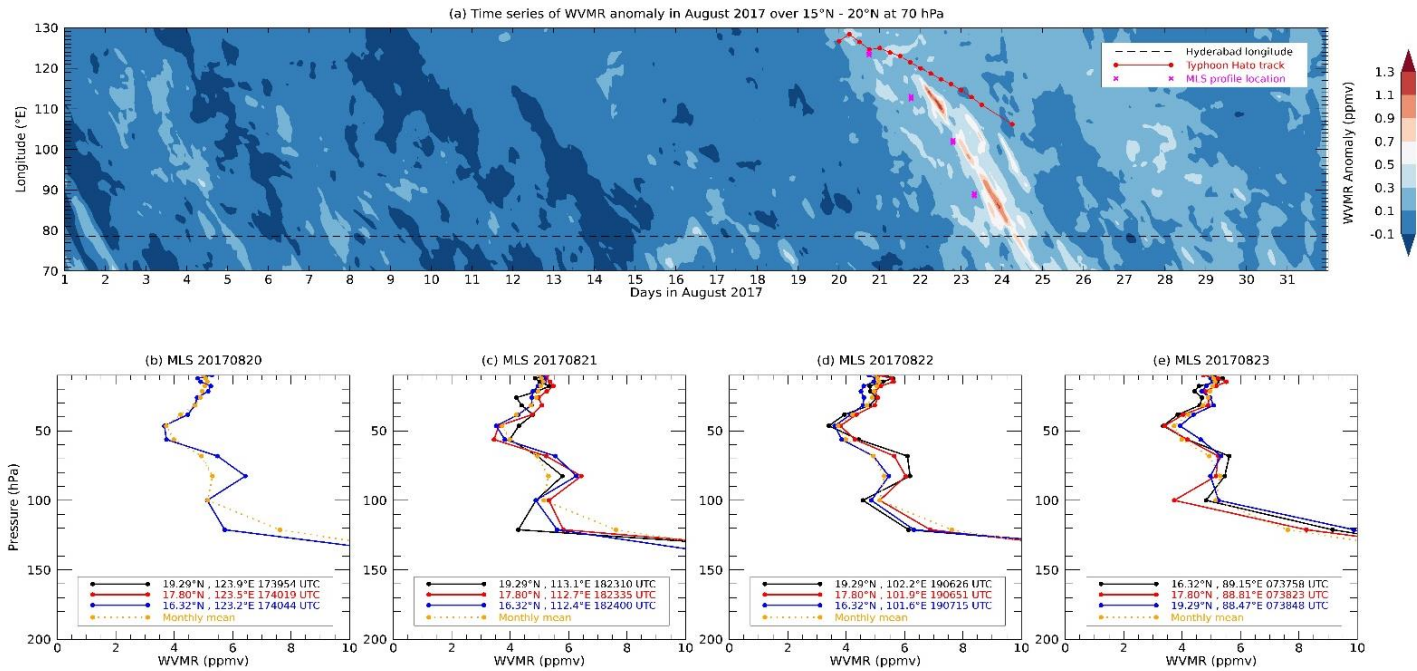
5 **Figure 10: (a) Hovmöller plot for the anomaly in water vapour mixing ratio (WVMR) derived from ERA5**
6 **temperature and relative humidity at 70 hPa pressure level for August 2017. Anomaly is computed by**
7 **subtracting the monthly mean WVMR for each grid between 15° N and 20° N. Dashed black line marks the**
8 **longitude of TIFR-BF in Hyderabad. Red dots represent the track of typhoon *Hato* while magenta crosses**
9 **show the location of nearest MLS profiles on different dates. Vertical profiles of WVMR from MLS between**
10 **15° N and 20° N observed on (b) 20 August 2017, (c) 21 August 2017, (d) 22 August 2017, and (e) 23 August**
11 **2017 at different times in UTC shown by different colours in the legend. The profiles affected by clouds are**
12 **filtered out. The orange line with orange circles in each panel represents the mean MLS profile for August**
13 **2017 obtained by averaging all profiles located in the region bounded by 15°-20° N and 70°-130° E.**

15 **3.4.3 In situ ice formation due to cooling induced by gravity waves associated with typhoon *Hato*.**

17 Figure 11 shows the temperature history of the air parcels along the back-trajectories initialized from the balloon

18 measurement site between 16 and 19 km altitude every hour. After being influenced by typhoon *Hato,* the air parcels

19 have experienced several cooling and warming phases before reaching the balloon site. We observe a quasi-periodic

20 occurrence of cold regions (represented by encircled regions in Fig. 11) with temperature below -81 °C along the

21 back-trajectories after being influenced by typhoon. Colder air parcels at these temperatures are susceptible to

22 generate supersaturation that can trigger the formation of ice crystals through ice nucleation. Near coincident and co-

23 located CATS and CALIOP observations on 22 and 23 August 2017, which intersected the back-trajectories, are

24 used to investigate the presence of cirrus clouds in these cold-regions. CATS and CALIOP observations on 23

25 August 2017 are almost coincident with the air parcels along the back-trajectories whereas CALIOP overpass on 22

August 2017 was a few hours later to the passage of the air parcels and thus, there is a difference in time (Fig. S7). It is interesting to see the presence of cirrus cloud layers with their base altitude greater than 16 km in and around these cold regions along the CALIPSO and CATS tracks.
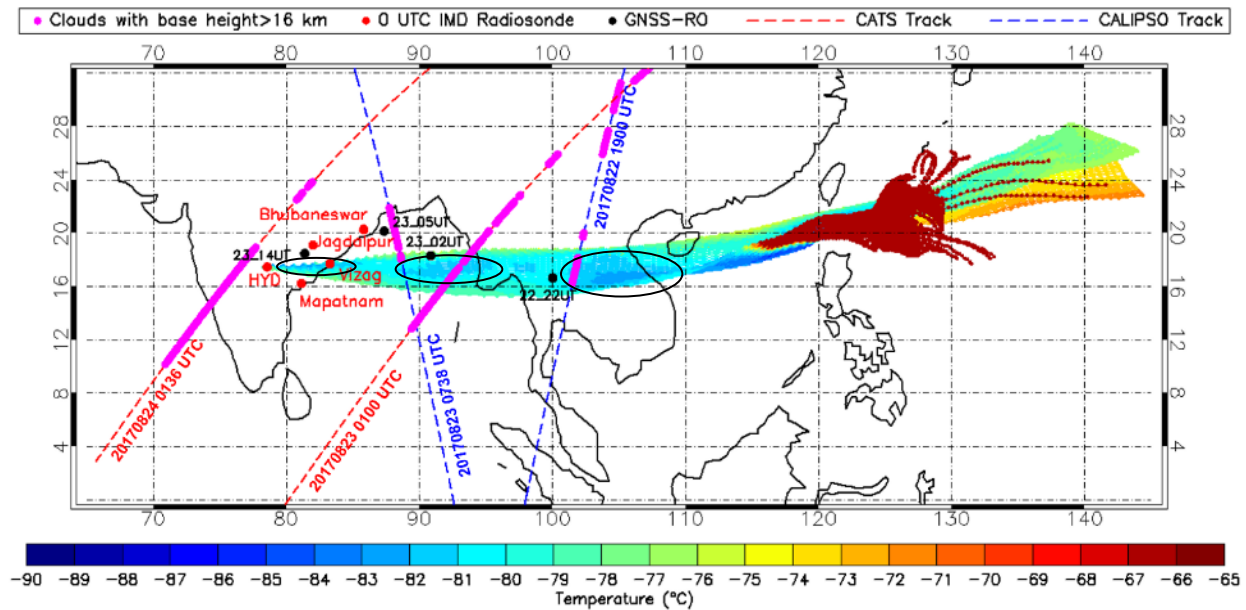
Figure 11: Filled coloured circles on the map show the temperature and location of the air parcel at every hour along the back-trajectories run from the balloon measurement sites between 16 and 19 km on 23 August 2017 at 20:00 UTC. The encircled regions along the back-trajectories represent quasi-periodic features with temperature below -81 °C. Red and blue dashed lines represent the nearest orbit tracks of CATS (on 24 August 2017 at 01:36 UTC and 23 August 2017 at 01:00 UTC) and CALIPSO (23 August 2017 at 07:38 UTC and 22 August 2017 at 19:00 UTC), respectively, with respect to the air parcels. Filled magenta circles superimposed on the orbit tracks represent the locations of cirrus cloud layer with base altitude greater than 16 km. Red filled circles on the map show the locations of the IMD stations from where daily radiosondes are launched at 00 UTC. Black filled circles show the locations of available GNSS-RO temperature profiles closest in time and space with CATS and CALIPSO overpasses.

The periodicity and the vertical extent of these cold regions can be clearly seen in Fig. 12 (a) where hourly temperature along the back-trajectories initialized from the balloon site between 16 and 19 km altitude at every 100 m has been shown as a function of altitude (and potential temperature, see Fig. S8). The periodic cold regions are confined in the altitude range between 16.5 and 18 km (potential temperature between 370 K and 400 K, see Fig. S8) containing the CPT. The anvil top height derived from Himawari-8 cloud-top temperature, which intersected the back-trajectories initialized between 16 and 19 km, is also superimposed (Fig. 12 a). The coldest temperatures are found over the strongest updraft regions of typhoon *Hato* with highest cloud tops reaching ~18.5 km. The occurrence of cirrus clouds between 16 and 18 km altitude in these cold regions is also clear from the near co-located and coincident measurements from CATS and CALIOP (Fig. 12 a). We observe westward propagating wave-like patterns in the temperature of the air parcels after they are influenced by typhoon *Hato*. There is also an upward propagation of these wave-patterns, which are more prominent near 18 km and altitudes above originating right from the region of typhoon *Hato*. Such periodic temperature fluctuations near the tropopause have also been observed along the diabatic back-trajectories (derived from ERA5 data) after being influenced by a typhoon

observed during the ASM in a recent study (Li et al., 2020). Li et al. (2020) investigated the influence of two typhoons on the dehydration and transport of low-ozone air masses near the tropopause during the ASM over Kunming, China using balloon measurements of temperature, ozone, and water vapour. However, such wave-like patterns in temperature and their role in cirrus cloud formation along the back-trajectories have not been discussed in their study. These wave-like temperature fluctuations or temperature anomalies near the tropopause could be due to the gravity waves generated by the deep convection associated with typhoon *Hato*.
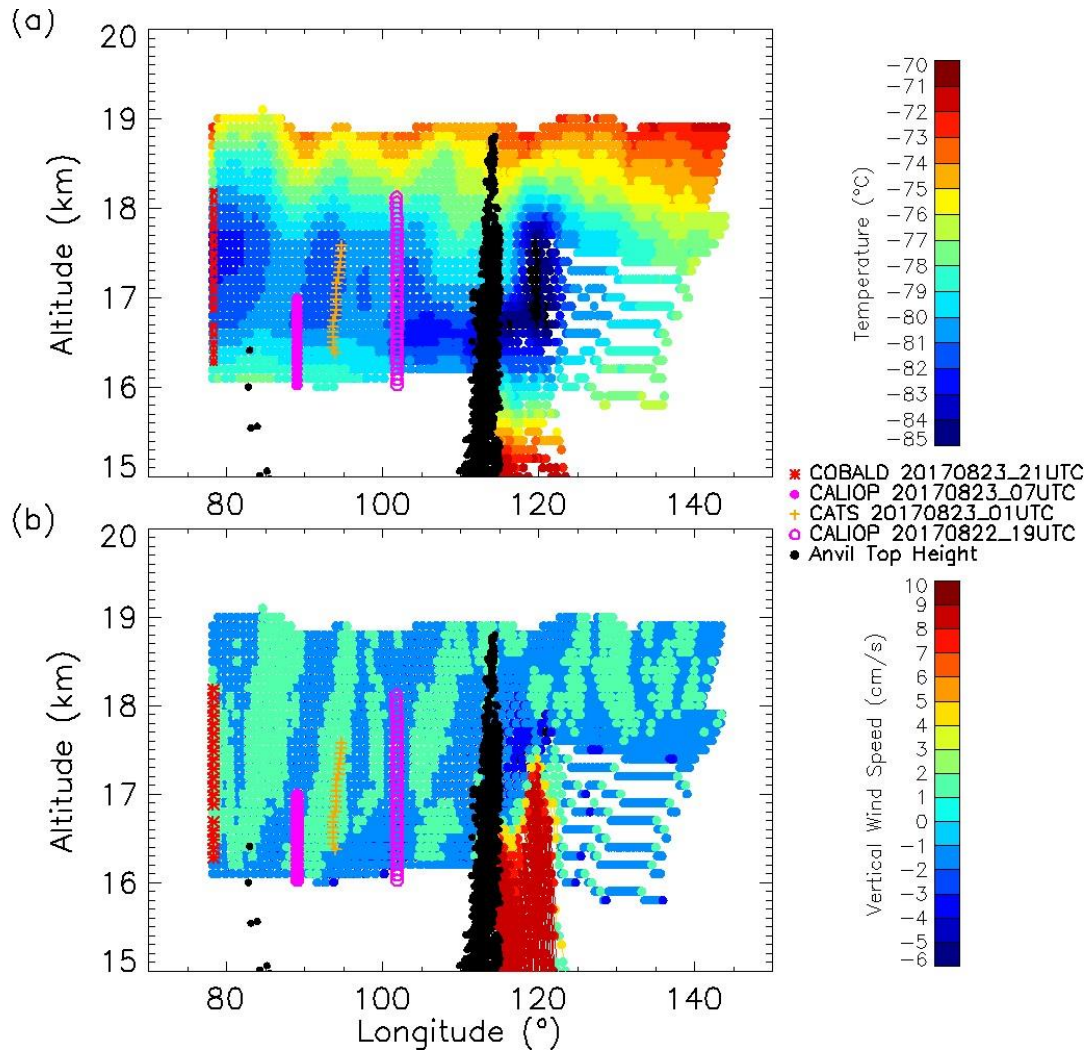
Figure 12: (a) Temperature history of the air parcels along the back-trajectories run from the balloon measurement sites between 16 and 19 km on 23 August 2017. Each filled coloured circle represents temperature value at every 100 m vertical resolution at each hour. (b) Same as (top) but for the vertical wind derived from the location and time of the back-trajectories. Different coloured symbols represent the location of the layered cirrus clouds observed near the tropopause from CALIOP, CATS and balloon measurements near co-located in space and time with respect to the back-trajectories. The locations of anvil cloud top altitude are represented by black dots.

We derived vertical wind speed along the back-trajectories (Fig. 12b) which shows correspondence between the periodic updrafts and cold anomalies. This suggests that the areas of cold anomalies are most likely formed due to the cooling induced by the updraft. It has been found that the updraft motion slows down the process of sedimentation, leading to longer lifetime of ice crystals in cirrus clouds (Podglajen et al., 2018). The downdrafts along the back-trajectories might have brought the moisture from the lower stratospheric hydration patch towards the CPT, resulting in secondary ice formation. This is evident from Fig. 5(b) where air parcels that originated between 17 and 17.5 km can be seen descending from higher altitudes at around 120° N. One more interesting point to note is that the ascent speed of the balloon has increased from ~6 m s^{-1} to ~8 m s^{-1} near the tropopause region (17.5-18.5 km) with its peak value at the top of CL5, above which it decreases sharply (see Fig. S9) and beyond that it exhibits oscillatory behaviour with increasing amplitude. It is interesting to note the presence of downdrafts (Fig. 12b) and sudden drop in balloon ascent speed above the CL5 top. Such vertical wind shear near the CPT could influence the ice nucleation with sudden rising motion triggering it while sinking motion inhibits it. The association of cold anomalies with updrafts indicate towards the possible role of gravity wave influence, which we investigate below.

The temperature along the back-trajectories in our analysis is obtained from the GEOS-FP reanalysis data, which may not be accurate enough to resolve these temperature fluctuations near the CPT when compared with the observations (Tegtmeier et al., 2020). To confirm the robustness of these cold anomalies, we use high resolution and relatively more accurate temperature observations from GNSS-RO near these colder regions. We found temperature profiles within 6 hours interval and within 400 km radius from the location of mean scattering ratio profiles of CATS and CALIOP intersecting the back-trajectories between 16° N and 18° N latitude band as shown in Fig. 13 (b), (c) and (d) arranged according to their observation time (from latest to farthest). The temperature near the tropopause is better resolved in the GNSS-RO temperature profiles as compared to the GMAO temperature profile averaged between 16° N and 18° N latitude band along the CATS and CALIOP orbit track. It is clear from the scattering ratio profiles obtained from the COBALD (at 940 nm, Fig. 13 a), CALIOP (at 532 nm, Fig. 13 b and d) and CATS (at 1064 nm, Fig. 13 c) that layered cirrus clouds or laminar cirrus are observed near the CPT in these cold anomalies. Profiles of RHi observed from the Aura-MLS on 22 and 23 August 2017 co-located with CALIOP show RHi values greater than 100 % at 100 hPa (~16.8 km) level, indicating supersaturation that resulted in ice formation (see Fig. S10).
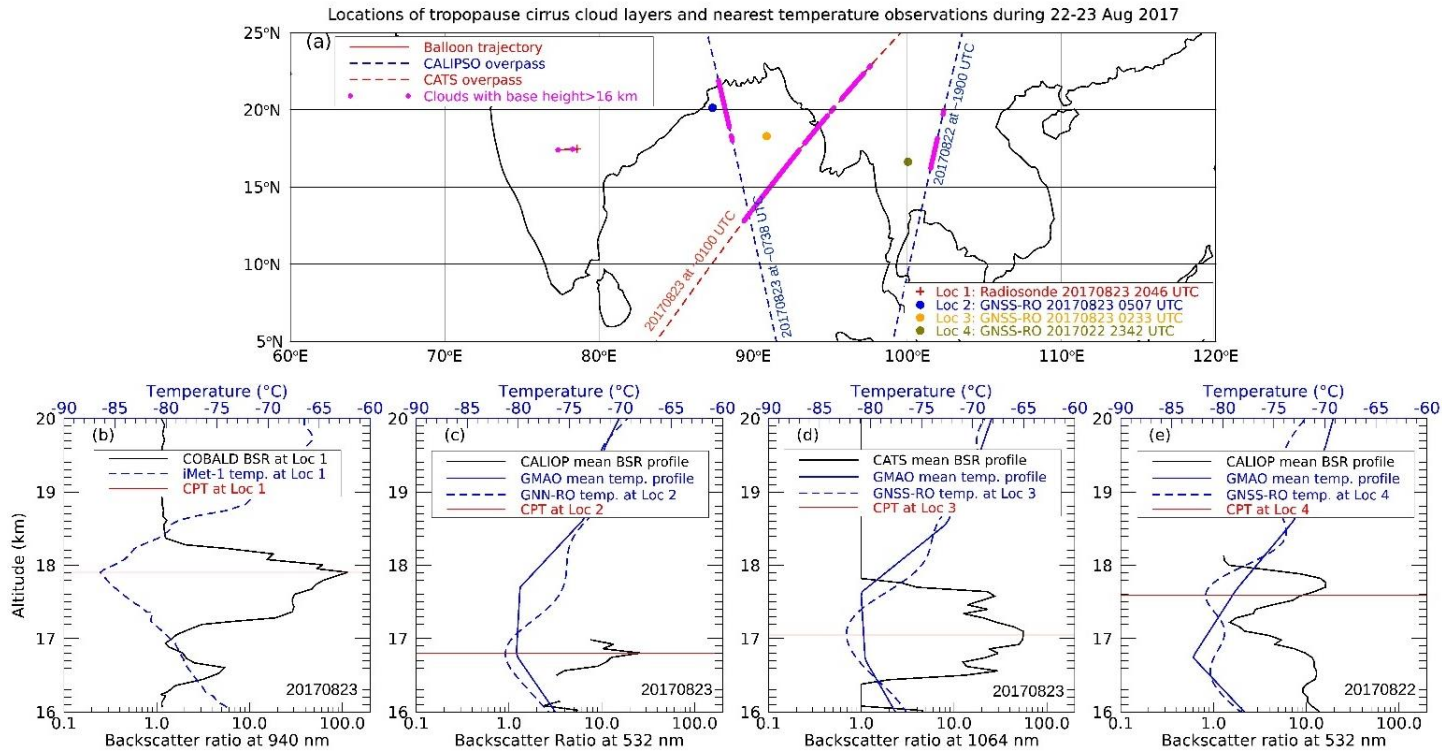
Figure 13: (a) Map showing the locations of tropopause cirrus clouds (magenta filled circles) observed along the balloon trajectory (solid red line), CATS (dashed red line) and CALIOP (dashed blue lines) overpasses on 22 and 23 August 2017. Vertical profile of backscatter ratio (shown by black line) obtained from (b) COBALD data on 23 August 2017 at around 20:40 UTC, (c) CALIOP on 23 August 2017 at around 07:38 UTC, (d) CATS on 23 August 2017 at around 00:59 UTC and (e) CALIOP on 22 August 2017 at around 19:07 UTC . CALIOP and CATS profiles are averaged between 17° and 18° N. Blue line in (c), (d) and (e) represents the mean temperature profile obtained by averaging the corresponding GMAO's GEOS-FP temperature profiles provided with CALIOP and CATS data. Dashed blue line shows the nearest available co-incident temperature profile obtained from (b) radiosonde measurement over location 1 (red plus symbol), (c) COSMIC GPS RO on 23 August 2017 at 05:07 UTC over location 2 (blue filled circle), (d) COSMIC GPS RO on 23 August 2017 at 02:33 UTC over location 3 (orange filled circle), (e) COSMIC GPS RO on 22 August 2017 at 23:42 UTC over location 4 (olive filled circle). The horizontal red line in each panel marks the CPT.

The CPT temperature and CPT altitude over Hyderabad (within 400 km radius around TIFR-BF) on 23 August 2017 exhibited a drastic change in the last 24 hours as observed from balloon and GNSS-RO observations as discussed earlier (in Table 3). Deep convective clouds that occurred over the land along the Indian East Coast in the late evening hours (as mentioned in Sect. 3.4.1) might also have helped in strengthening this tropopause cooling. CPT temperature was minimum and CPT altitude was maximum for this BATAL flight. All the IMD stations near
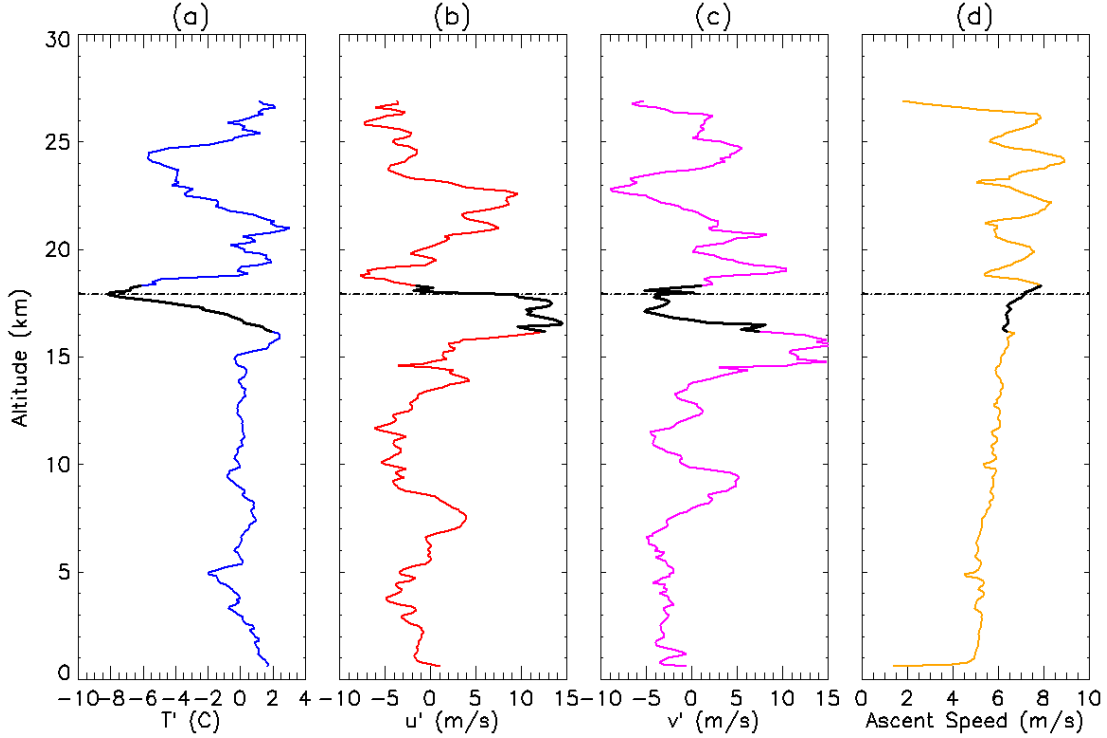
2 **Figure 14: Vertical profile of (a) temperature anomaly, (b) zonal wind speed anomaly, (c) meridional wind**
3 **speed anomaly and (d) ascent speed of the balloon observed on 23 August 2017. Anomalies are estimated by**
4 **subtracting the monthly mean profile from the profile obtained on 23 August 2017. Mean profiles are**
5 **obtained from all the radiosonde profiles at 00 UTC and BATAL flights over Hyderabad for August 2017.**
6 **The black dashed horizontal line in each panel denotes the location of the CPT (at 17.9 km) observed on 23**
7 **August 2017 at around 21:00 UTC from the balloon. Black shading in each profile shows the location of the**
8 **tropopause cirrus cloud.**

10 Hyderabad (Machilipatnam, Vizag, and Jagdalpur) recorded lower tropopause temperature on 24 August 2017 at 00

11 UTC compared to that observed on 23 August 2017 at 00 UTC. The magnitude of tropopause cooling can be

12 expressed in terms of anomaly in the observed temperature with respect to the mean observed temperature over

13 Hyderabad. We construct a mean temperature profile over Hyderabad region during August 2017 using the

14 temperature profiles obtained from all (nine) the flights of BATAL-2017 campaign over TIFR-BF and daily 00 UTC

15 radiosonde data from Hyderabad airport. The vertical profile of the observed temperature anomaly for our balloon

16 flight on 23 August 2017 estimated after subtracting the mean temperature profile from it clearly shows a cold

17 anomaly of ~ -8 °C) near the CPT region (Fig. 14 a) where CL5 was found. We also notice a wave-like pattern in the

18 temperature anomaly profile above 15 km altitude. Using the airborne data from the ATTREX campaign, Kim et al.

19 (2016) showed that about 86% of the cirrus clouds between 16.5 and 18 km over the Pacific are formed in the cold

20 anomalies induced by gravity waves. They also found that these clouds more often form in the negative slope of the

21 temperature anomaly, which is also true for CL5 (see the cloud shading in Fig. 14) but it is also present in the

22 positive anomaly above the tropopause as well up to the CL5 top altitude where ascent speed peaks and drops (see

23 Fig. 14d). Similar wave like pattern is also noticed in the anomaly profiles of zonal and meridional wind speed (Fig.

24 14b and 14c), estimated by subtracting the mean zonal and meridional speeds for August 2017 obtained from

BATAL flights and Hyderabad airport radiosonde data for August 2017. Such wave pattern is also reflected in the spatial movement of the balloon as shown in Fig. S1. In addition to this, the ascent speed of the balloon also shows oscillation above the CPT with its amplitude increasing with altitude (Fig. 14d). All these observations indicate towards the possible influence of gravity waves in the tropopause cooling, which possibly led to ice formation after reaching supersaturation with respect to ice. Recently, Martínez et al. (2021) have reported a case of extremely thin cirrus cloud layer formed near the CPT over the Southwestern Indian Ocean using COBALD and CFH observations. Using the spectral analysis (S-transform, Stockwell et al. (1996)) of temperature anomaly and ascent speed, they suggested the role of homogeneous freezing under the influence of a high frequency gravity wave with a vertical wavelength of 1.5 km. Using Hodograph analysis of radiosonde data following Leena et al. (2012), we estimated the gravity wave characteristics. We found that the gravity wave was propagating from south-east direction to north-west direction in the stratosphere (18-26 km) with a horizontal phase speed of about 18.8 m s^{-1} and a horizontal wavelength of about 1770 km, confirming that it was generated from typhoon *Hato.*

4 Summary

In situ measurements in cirrus clouds with ice crystals smaller than 100 μm near the tropopause over the ASM region are sparse, and the available observations mainly come from probes on aircraft that are traveling at rapid speeds through the clouds, leading to shattering of ice crystals and failure to resolve small ice crystal habits. In this paper, we have presented balloon-borne measurements of the optical and microphysical properties of a tropical tropopause cirrus cloud layer obtained using a backscatter sonde and an optical particle counter on 23 August 2017 during the BATAL campaign over Hyderabad, India. This layer was a subvisible cirrus cloud located at an extremely cold tropopause temperature of -86.4 ℃. The top of this layer was found in the lower stratosphere at about 18.3 km. Ice crystals in this cloud layer were smaller than 50 μm in diameter. Nearby lidar backscatter measurements from the CATS onboard ISS confirmed the presence of this tropopause cirrus that extended more than 500 km along the ISS orbit track. IWC for this layer was estimated independently from the backscatter measurements and optical particle counter and found to be less than 0.2 mg m^{-3}. Simultaneous measurements of backscatter coefficient from COBALD and extinction coefficient derived from Boulder Counter measurements allowed us to derive a range-resolved lidar ratio for this tropopause cirrus cloud layer, whose average value is 32.18±6.73 sr .We demonstrated that the combination of COBALD and Boulder Counter can be used to estimate range-resolved lidar ratios for tropopause cirrus cloud layers, which may prove useful in validating lidar retrievals of extinction coefficient. This estimate can be improved with higher ice particle sampling rate at more size channels especially at smaller radii. We also investigated the formation mechanism of this layer using back-trajectories, satellite, and ERA5 reanalysis data. Back-trajectories from the balloon measurement site and their intersection with convective clouds observed in Himawai-8 brightness temperature images suggest that the layer was influenced by a category-3 typhoon named *Hato*. Both Himawari-8 and CALIOP observations showed that *Hato* injected ice crystals into the lower stratosphere causing a hydration patch as revealed by ERA5 WVMR and confirmed by the MLS WVMR observations. These moist plumes were seen to be advected by the ASM anticyclonic flow towards

Hyderabad. Moreover, along the back-trajectories there were quasi-periodic cold and warm anomalies near the CPT associated with updrafts and downdrafts, respectively. CATS and CALIOP observations showed the presence of tropopause cirrus clouds in these cold anomalies. These perturbations are most likely caused by the gravity waves induced by typhoon *Hato*. Signatures of such perturbations were also noticed in the temperature and wind profiles obtained from our balloon observations. Through this case study, we conclude that the overshooting clouds in typhoons can cause direct stratospheric hydration during the ASM in addition to the usual overshooting convective systems. Following the ASM anticyclonic flow, this stratospheric hydration can get advected several thousands of kilometres and subsequently may lead to tropopause cirrus clouds upon cooling induced by typhoon induced gravity waves.

The occurrence frequency of tropopause-penetrating deep convective clouds (Aumann et al., 2018) and the intensity of tropical cyclones are expected to increase in a warmer climate (Stocker et al., 2013; Emanuel, 2005), which in turn are likely to increase the occurrence of ice-injections with consequences for the stratospheric composition, thin tropopause cirrus clouds and further feedbacks on the global climate (Dessler et al., 2016; Solomon et al., 2010). A recent modelling study (Smith et al., 2022) has found that the impact of convective hydration in response to increased CO_2 depends not only on the frequency and penetration altitude of convective overshooting into the stratosphere but also on large-scale temperatures in the TTL. In this context, the occurrence of frequent deep convection and presence of cold temperatures in the TTL over the ASM anticyclone region are important for convective hydration and tropopause cirrus cloud formation. In future, simultaneous measurements of temperature, water vapour, and the microphysical properties of cirrus clouds using quasi-isentropic balloon flights within the coldest regions of the ASM anticyclone will be planned to obtain a detailed understanding of the impacts of overshooting convection on the formation of tropical tropopause cirrus clouds.

Appendix A

A1 Data and Methods

Compact Optical Backscatter AerosoL Detector (COBALD)

COBALD consists of two high power (500 mW) Light Emitting Diodes (LEDs) which emit light at 455 nm (blue) and 940 nm (near infrared) wavelengths. A silicon photodiode placed between the two LEDs collects the light backscattered from the air-borne particles (molecules, aerosols, and clouds). When connected with an iMet radiosonde, the instrument adds backscatter and monitor signals at both wavelengths to the radiosonde pressure, temperature, relative humidity, wind speed and wind direction data at a rate of 1 Hz to the receiving ground station. The concurrent profiles of pressure, temperature and backscattered counts are used to calculate backscatter ratio (BSR), the ratio of total (molecules and particulate) backscatter coefficient ($\beta = \beta_p + \beta_m$) to the molecular backscatter coefficient (β_m) at a given wavelength. The BSR is calibrated in a region of the atmosphere minimally affected by aerosols and adjusted with a reference density signal derived from pressure and temperature. The absolute error associated with BSR is within 5 % while its precision is better than 1 % in the UTLS region (Vernier et al., 2015).

Lidar ratio

The ratio of extinction to backscatter coefficient, often called the lidar ratio, is used in retrieving extinction coefficient from the backscatter measurements of elastic backscatter lidars. The retrieved extinction coefficient and hence the layer optical thickness are very sensitive to the magnitude of the lidar ratio used in the extinction retrieval, which depends on the number concentration, size and shape distributions and refractive index of the particles (Ackermann, 1998). Since microphysical properties of cirrus clouds mainly depend on temperature and RHi (Heymsfield et al., 2017), it is essential to study the dependence of lidar ratio on these factors. The variation of lidar ratio within a cirrus cloud layer can be measured in situ or by using inelastic lidars, such as Raman lidars (Ansmann et al., 1992; Sakai et al., 2003) or high spectral resolution lidars (Grund and Eloranta, 1990). In case of elastic backscatter lidars, for an extinction coefficient retrieval the lidar ratio is usually assumed to be constant (range-independent) inside a cirrus cloud layer. Version 3 CATS lidar clouds products use a constant lidar ratio of 28 sr over land and 32 sr over the oceans for tropical ice clouds (CATS Data Release Notes Version 3.0, 2018). This approach of using a constant lidar ratio is unable to account for the natural variability of the actual lidar ratio leading to erroneous extinction coefficient and cloud optical thickness retrievals for cirrus clouds (Saito et al., 2017). Using multi-year nighttime CALIOP two-way transmission and collocated IIR absorption optical depth at 12.05 µm for single-layer semi-transparent cirrus cloud layers over the ocean, Garnier et al. (2015) derived temperature dependent multiple-scattering factor and a corresponding temperature-dependent parametrization of initial lidar ratio. Following this study, the multiple scattering factor and lidar ratio in CALIOP V4 algorithm are approximated by a sigmoid function of the centroid temperature of the 532 nm attenuated coefficient within the cloud layer (Young et al., 2018). According to this sigmoid function, the value of initial lidar ratio for a cirrus cloud layer with centroid temperature between -80 °C and -90 °C falls in the range of 20-22 sr. The introduction of this approach in the CALIOP V4 algorithm has resulted in the reduction of the relative uncertainty assigned to the initial lidar ratio for semi-transparent ice clouds by 15 % compared to V3 algorithm (Young et al., 2018).

There are many studies on lidar ratio of cirrus clouds using lidars measurements (see Table 5 of Voudouri et al. (2020)) but such studies using in situ measurements of subvisible cirrus clouds near the tropical tropopause are rare. Our unique balloon measurements provided us independent in situ measurements of backscatter (from COBALD) and extinction coefficients (from Boulder Counter) inside a subvisible cirrus layer near the CPT which allowed us to estimate the vertical profile of lidar ratio as shown in Table 2.

Data availability

CALIPSO data were obtained from NASA Langley Research Centre Atmospheric Science Data Centre (https://asdc.larc.nasa.gov/project/CALIPSO), GEOS-5 FP wind data from NASA GMAO and Himawari-8 data from the University of Wisconsin - Madison Space Science and Engineering Centre (SSEC). Doppler weather radar data were obtained from India Meteorological Department (IMD). Daily 00 UTC radiosonde data were obtained from University of Wyoming (https://weather.uwyo.edu/upperair/sounding.html), GNSS-RO temperature profile data from UCAR-COSMIC (https://cdaac-www.cosmic.ucar.edu/), ERA5 reanalysis data from Copernicus climate data store (https://cds.climate.copernicus.eu/cdsapp#!/dataset/reanalysis-era5-single-levels?tab=overview), Aura-

MLS data from NASA-JPL (https://disc.gsfc.nasa.gov/datasets/ML2RHI_004/summary) and CATS data from NASA-GSFC (https://cats.gsfc.nasa.gov/). BATAL data will be made available at https://science-data.larc.nasa.gov/BATAL/data.html and can also be obtained through request.

Author contribution

AKP wrote the manuscript draft. JPV, TDF, BSK, HG, MVR, AKP and AJ organized the field campaign. AKP and JPV collected in situ data. TDF and HG provided back trajectories. AKP and JPV analysed in situ and back-trajectory data. KMB provided cloud top heights from Himawari-8 along the back-trajectories. MAA contributed to CALIPSO data analysis. AKP analysed CATS, CALIPSO, MLS, GNSS-RO and ERA5 data. FGW provided calibrated COBALD data. SD contributed to ERA5 data analysis. KAJ provided doppler weather radar analysis. MVR provided gravity wave characteristics. All the authors reviewed and edited the manuscript.

Competing interests

The authors declare that they have no conflict of interest.

Acknowledgements

This paper is dedicated to our great colleagues Mr. B. Suneel Kumar and Dr. T. Duncan Fairlie who made significant contributions to the BATAL project and left us much too early. This work was carried out under ISRO-NASA joint project called BATAL. The 2017 balloon deployment and the analysis of the data were supported by the NASA ROSES Upper Atmospheric Research and the Upper Atmospheric Composition Observations programs through an IDIQ task at NASA Langley Research Centre. AKP is thankful to the Physical Research Laboratory in Ahmedabad, India for supporting his participation in the BATAL-2017 field campaign. He is also thankful for the support provided by the NASA Postdoctoral Program (NPP) fellowship administered by Universities Space Research Association, NASA Langley Research Centre, and National Institute of Aerospace in conducting this research. We thank the engineers, technicians, and staffs at TIFR Balloon Facility in Hyderabad and National Atmospheric Research Laboratory at Gadanki, India for their valuable contributions towards the scientific, technical, and logistical support provided during the BATAL campaign. We also thank Mijeong Park from NCAR for helpful discussion.

References

Ackermann, J.: The Extinction-to-Backscatter Ratio of Tropospheric Aerosol: A Numerical Study, Journal of Atmospheric and Oceanic Technology, 15, 1043–1050, https://doi.org/10.1175/1520-0426(1998)015<1043:TETBRO>2.0.CO;2, 1998.

Ansmann, A., Wandinger, U., Riebesell, M., Weitkamp, C., and Michaelis, W.: Independent measurement of extinction and backscatter profiles in cirrus clouds by using a combined Raman elastic-backscatter lidar, Appl. Opt., AO, 31, 7113–7131, https://doi.org/10.1364/AO.31.007113, 1992.

Anthes, R. A., Bernhardt, P. A., Chen, Y., Cucurull, L., Dymond, K. F., Ector, D., Healy, S. B., Ho, S.-P., Hunt, D. C., Kuo, Y.-H., Liu, H., Manning, K., McCormick, C., Meehan, T. K., Randel, W. J., Rocken, C., Schreiner, W. S., Sokolovskiy, S. V., Syndergaard, S., Thompson, D. C., Trenberth, K. E., Wee, T.-K., Yen, N. L., and Zeng, Z.: The COSMIC/FORMOSAT-3 Mission: Early Results, Bulletin of the American Meteorological Society, 89, 313–334, https://doi.org/10.1175/BAMS-89-3-313, 2008.

Aumann, H. H., Behrangi, A., and Wang, Y.: Increased Frequency of Extreme Tropical Deep Convection: AIRS Observations and Climate Model Predictions, Geophysical Research Letters, 45, 13,530-13,537, https://doi.org/10.1029/2018GL079423, 2018.

Baumgardner, D., Abel, S. J., Axisa, D., Cotton, R., Crosier, J., Field, P., Gurganus, C., Heymsfield, A., Korolev, A., Krämer, M., Lawson, P., McFarquhar, G., Ulanowski, Z., and Um, J.: Cloud Ice Properties: In Situ Measurement Challenges, Meteorological Monographs, 58, 9.1-9.23, https://doi.org/10.1175/AMSMONOGRAPHS-D-16-0011.1, 2017.

Bedka, K. M. and Khlopenkov, K.: A Probabilistic Multispectral Pattern Recognition Method for Detection of Overshooting Cloud Tops Using Passive Satellite Imager Observations, Journal of Applied Meteorology and Climatology, 55, 1983–2005, https://doi.org/10.1175/JAMC-D-15-0249.1, 2016.

Bessho, K., Date, K., Hayashi, M., Ikeda, A., Imai, T., Inoue, H., Kumagai, Y., Miyakawa, T., Murata, H., Ohno, T., Okuyama, A., Oyama, R., Sasaki, Y., Shimazu, Y., Shimoji, K., Sumida, Y., Suzuki, M., Taniguchi, H., Tsuchiyama, H., Uesawa, D., Yokota, H., and Yoshida, R.: An Introduction to Himawari-8/9— Japan's New-Generation Geostationary Meteorological Satellites, Journal of the Meteorological Society of Japan. Ser. II, 94, 151–183, https://doi.org/10.2151/jmsj.2016-009, 2016.

Biondi, R., Ho, S.-P., Randel, W., Syndergaard, S., and Neubert, T.: Tropical cyclone cloud-top height and vertical temperature structure detection using GPS radio occultation measurements, Journal of Geophysical Research: Atmospheres, 118, 5247–5259, https://doi.org/10.1002/jgrd.50448, 2013.

Biondi, R., Steiner, A. K., Kirchengast, G., and Rieckh, T.: Characterization of thermal structure and conditions for overshooting of tropical and extratropical cyclones with GPS radio occultation, Atmospheric Chemistry and Physics, 15, 5181–5193, https://doi.org/10.5194/acp-15-5181-2015, 2015.

Biondi, R., Steiner, A. K., Kirchengast, G., Brenot, H., and Rieckh, T.: Supporting the detection and monitoring of volcanic clouds: A promising new application of Global Navigation Satellite System radio occultation, Advances in Space Research, 60, 2707–2722, https://doi.org/10.1016/j.asr.2017.06.039, 2017.

Bourgeois, Q., Ekman, A. M. L., Igel, M. R., and Krejci, R.: Ubiquity and impact of thin mid-level clouds in the tropics, Nat Commun, 7, 12432, https://doi.org/10.1038/ncomms12432, 2016.

Brabec, M., Wienhold, F. G., Luo, B. P., Vömel, H., Immler, F., Steiner, P., Hausammann, E., Weers, U., and Peter, T.: Particle backscatter and relative humidity measured across cirrus clouds and comparison with microphysical cirrus modelling, Atmospheric Chemistry and Physics, 12, 9135–9148, https://doi.org/10.5194/acp-12-9135-2012, 2012.

Brunamonti, S., Jorge, T., Oelsner, P., Hanumanthu, S., Singh, B. B., Kumar, K. R., Sonbawne, S., Meier, S., Singh, D., Wienhold, F. G., Luo, B. P., Boettcher, M., Poltera, Y., Jauhiainen, H., Kayastha, R., Karmacharya, J., Dirksen, R., Naja, M., Rex, M., Fadnavis, S., and Peter, T.: Balloon-borne measurements of temperature, water vapor, ozone and aerosol backscatter on the southern slopes of the Himalayas during StratoClim 2016–2017, Atmospheric Chemistry and Physics, 18, 15937–15957, https://doi.org/10.5194/acp-18-15937-2018, 2018.

Brunamonti, S., Füzér, L., Jorge, T., Poltera, Y., Oelsner, P., Meier, S., Dirksen, R., Naja, M., Fadnavis, S., Karmacharya, J., Wienhold, F. G., Luo, B. P., Wernli, H., and Peter, T.: Water Vapor in the Asian Summer Monsoon Anticyclone: Comparison of Balloon-Borne Measurements and ECMWF Data, Journal of Geophysical Research: Atmospheres, 124, 7053–7068, https://doi.org/10.1029/2018JD030000, 2019.

Brunamonti, S., Martucci, G., Romanens, G., Poltera, Y., Wienhold, F. G., Hervo, M., Haefele, A., and Navas-Guzmán, F.: Validation of aerosol backscatter profiles from Raman lidar and ceilometer using balloon-borne measurements, Atmospheric Chemistry and Physics, 21, 2267–2285, https://doi.org/10.5194/acp-21-2267-2021, 2021.

Cirisan, A., Luo, B. P., Engel, I., Wienhold, F. G., Sprenger, M., Krieger, U. K., Weers, U., Romanens, G., Levrat, G., Jeannet, P., Ruffieux, D., Philipona, R., Calpini, B., Spichtinger, P., and Peter, T.: Balloon-borne match measurements of midlatitude cirrus clouds, Atmospheric Chemistry and Physics, 14, 7341–7365, https://doi.org/10.5194/acp-14-7341-2014, 2014.

Corti, T., Luo, B. P., de Reus, M., Brunner, D., Cairo, F., Mahoney, M. J., Martucci, G., Matthey, R., Mitev, V., dos Santos, F. H., Schiller, C., Shur, G., Sitnikov, N. M., Spelten, N., Vössing, H. J., Borrmann, S., and Peter, T.: Unprecedented evidence for deep convection hydrating the tropical stratosphere, Geophysical Research Letters, 35, https://doi.org/10.1029/2008GL033641, 2008.

Dessler, A. e., Ye, H., Wang, T., Schoeberl, M. r., Oman, L. d., Douglass, A. r., Butler, A. h., Rosenlof, K. h., Davis, S. m., and Portmann, R. w.: Transport of ice into the stratosphere and the humidification of the stratosphere over the 21st century, Geophysical Research Letters, 43, 2323–2329, https://doi.org/10.1002/2016GL067991, 2016.

Dzambo, A. M., Hitchman, M. H., and Chang, K.-W.: The Influence of Gravity Waves on Ice Saturation in the Tropical Tropopause Layer over Darwin, Australia, Atmosphere, 10, 778, https://doi.org/10.3390/atmos10120778, 2019.

Emanuel, K.: Increasing destructiveness of tropical cyclones over the past 30 years, Nature, 436, 686–688, https://doi.org/10.1038/nature03906, 2005.

Fairlie, T. D., Szykman, J., Gilliland, A., Bradley Pierce, R., Kittaka, C., Weber, S., Engel-Cox, J., Rogers, R. R., Tikvart, J., Scheffe, R., and Dimmick, F.: Lagrangian sampling of 3-D air quality model results for regional transport contributions to sulfate aerosol concentrations at Baltimore, MD, in summer 2004, Atmospheric Environment, 43, 3275–3288, https://doi.org/10.1016/j.atmosenv.2009.02.026, 2009.

Fairlie, T. D., Vernier, J.-P., Natarajan, M., and Bedka, K. M.: Dispersion of the Nabro volcanic plume and its relation to the Asian summer monsoon, Atmospheric Chemistry and Physics, 14, 7045–7057, https://doi.org/10.5194/acp-14-7045-2014, 2014.

Foot, J. S.: Some observations of the optical properties of clouds. II: Cirrus, Quarterly Journal of the Royal Meteorological Society, 114, 145–164, https://doi.org/10.1002/qj.49711447908, 1988.

Fu, Q. and Liou, K. N.: Parameterization of the Radiative Properties of Cirrus Clouds, Journal of the Atmospheric Sciences, 50, 2008–2025, https://doi.org/10.1175/1520-0469(1993)050<2008:POTRPO>2.0.CO;2, 1993.

Garnier, A., Pelon, J., Vaughan, M. A., Winker, D. M., Trepte, C. R., and Dubuisson, P.: Lidar multiple scattering factors inferred from CALIPSO lidar and IIR retrievals of semi-transparent cirrus cloud optical depths over oceans, Atmos. Meas. Tech., 8, 2759–2774, https://doi.org/10.5194/amt-8-2759-2015, 2015.

Gasparini, B. and Lohmann, U.: Why cirrus cloud seeding cannot substantially cool the planet, Journal of Geophysical Research: Atmospheres, 121, 4877–4893, https://doi.org/10.1002/2015JD024666, 2016.

Grund, C. J. and Eloranta, E. W.: The 27–28 October 1986 FIRE IFO Cirrus Case Study: Cloud Optical Properties Determined by High Spectral Resolution Lidar, Monthly Weather Review, 118, 2344–2355, https://doi.org/10.1175/1520-0493(1990)118<2344:TOFICC>2.0.CO;2, 1990.

He, Q., Ma, J., Zheng, X., Yan, X., Vömel, H., Wienhold, F. G., Gao, W., Liu, D., Shi, G., and Cheng, T.: Observational evidence of particle hygroscopic growth in the upper troposphere–lower stratosphere (UTLS) over the Tibetan Plateau, Atmos. Chem. Phys., 19, 8399–8406, https://doi.org/10.5194/acp-19-8399-2019, 2019.

He, Q. S., Li, C. C., Ma, J. Z., Wang, H. Q., Shi, G. M., Liang, Z. R., Luan, Q., Geng, F. H., and Zhou, X. W.: The Properties and Formation of Cirrus Clouds over the Tibetan Plateau Based on Summertime Lidar Measurements, Journal of the Atmospheric Sciences, 70, 901–915, https://doi.org/10.1175/JAS-D-12-0171.1, 2013.

Hersbach, H., Bell, B., Berrisford, P., Hirahara, S., Horányi, A., Muñoz-Sabater, J., Nicolas, J., Peubey, C., Radu, R., Schepers, D., Simmons, A., Soci, C., Abdalla, S., Abellan, X., Balsamo, G., Bechtold, P., Biavati, G., Bidlot, J., Bonavita, M., De Chiara, G., Dahlgren, P., Dee, D., Diamantakis, M., Dragani, R., Flemming, J., Forbes, R., Fuentes, M., Geer, A., Haimberger, L., Healy, S., Hogan, R. J., Hólm, E., Janisková, M., Keeley, S., Laloyaux, P., Lopez, P., Lupu, C., Radnoti, G., de Rosnay, P., Rozum, I., Vamborg, F., Villaume, S., and Thépaut, J.-N.: The ERA5 global reanalysis, Quarterly Journal of the Royal Meteorological Society, 146, 1999–2049, https://doi.org/10.1002/qj.3803, 2020.

Heymsfield, A., Winker, D., Avery, M., Vaughan, M., Diskin, G., Deng, M., Mitev, V., and Matthey, R.: Relationships between Ice Water Content and Volume Extinction Coefficient from In Situ Observations for Temperatures from 0° to −86°C: Implications for Spaceborne Lidar Retrievals, Journal of Applied Meteorology and Climatology, 53, 479–505, https://doi.org/10.1175/JAMC-D-13-087.1, 2014.

Heymsfield, A. J. and Westbrook, C. D.: Advances in the Estimation of Ice Particle Fall Speeds Using Laboratory and Field Measurements, Journal of the Atmospheric Sciences, 67, 2469–2482, https://doi.org/10.1175/2010JAS3379.1, 2010.

Heymsfield, A. J., Krämer, M., Luebke, A., Brown, P., Cziczo, D. J., Franklin, C., Lawson, P., Lohmann, U., McFarquhar, G., Ulanowski, Z., and Tricht, K. V.: Cirrus Clouds, Meteorological Monographs, 58, 2.1-2.26, https://doi.org/10.1175/AMSMONOGRAPHS-D-16-0010.1, 2017.

Hong, Y., Liu, G., and Li, J.-L. F.: Assessing the Radiative Effects of Global Ice Clouds Based on CloudSat and CALIPSO Measurements, Journal of Climate, 29, 7651–7674, https://doi.org/10.1175/JCLI-D-15-0799.1, 2016.

Höpfner, M., Ungermann, J., Borrmann, S., Wagner, R., Spang, R., Riese, M., Stiller, G., Appel, O., Batenburg, A. M., Bucci, S., Cairo, F., Dragoneas, A., Friedl-Vallon, F., Hünig, A., Johansson, S., Krasauskas, L., Legras, B., Leisner, T., Mahnke, C., Möhler, O., Molleker, S., Müller, R., Neubert, T., Orphal, J., Preusse, P., Rex, M., Saathoff, H., Stroh, F., Weigel, R., and Wohltmann, I.: Ammonium nitrate particles formed in upper troposphere from ground ammonia sources during Asian monsoons, Nat. Geosci., 12, 608–612, https://doi.org/10.1038/s41561-019-0385-8, 2019.

Horinouchi, T., Shimada, U., and Wada, A.: Convective Bursts With Gravity Waves in Tropical Cyclones: Case Study With the Himawari-8 Satellite and Idealized Numerical Study, Geophysical Research Letters, 47, e2019GL086295, https://doi.org/10.1029/2019GL086295, 2020.

Jensen, E. J., Toon, O. B., Pfister, L., and Selkirk, H. B.: Dehydration of the upper troposphere and lower stratosphere by subvisible cirrus clouds near the tropical tropopause, Geophysical Research Letters, 23, 825–828, https://doi.org/10.1029/96GL00722, 1996.

Jensen, E. J., Pfister, L., Jordan, D. E., Bui, T. V., Ueyama, R., Singh, H. B., Thornberry, T. D., Rollins, A. W., Gao, R.-S., Fahey, D. W., Rosenlof, K. H., Elkins, J. W., Diskin, G. S., DiGangi, J. P., Lawson, R. P., Woods, S., Atlas, E. L., Rodriguez, M. A. N., Wofsy, S. C., Pittman, J., Bardeen, C. G., Toon, O. B., Kindel, B. C., Newman, P. A., McGill, M. J., Hlavka, D. L., Lait, L. R., Schoeberl, M. R., Bergman, J. W., Selkirk, H. B., Alexander, M. J., Kim, J.-E., Lim, B. H., Stutz, J., and Pfeilsticker, K.: The NASA Airborne Tropical Tropopause Experiment: High-Altitude Aircraft Measurements in the Tropical Western Pacific, Bulletin of the American Meteorological Society, 98, 129–143, https://doi.org/10.1175/BAMS-D-14-00263.1, 2017.

Jensen, E. J., Pan, L. L., Honomichl, S., Diskin, G. S., Krämer, M., Spelten, N., Günther, G., Hurst, D. F., Fujiwara, M., Vömel, H., Selkirk, H. B., Suzuki, J., Schwartz, M. J., and Smith, J. B.: Assessment of Observational Evidence for Direct Convective Hydration of the Lower Stratosphere, Journal of Geophysical Research: Atmospheres, 125, e2020JD032793, https://doi.org/10.1029/2020JD032793, 2020.

Jiang, B., Lin, W., Hu, C., and Wu, Y.: Tropical cyclones impact on tropopause and the lower stratosphere vapour based on satellite data, Atmospheric Science Letters, 21, e1006, https://doi.org/10.1002/asl.1006, 2020.

Kärcher, B.: Cirrus Clouds and Their Response to Anthropogenic Activities, Curr Clim Change Rep, 3, 45–57, https://doi.org/10.1007/s40641-017-0060-3, 2017.

Khaykin, S., Lukyanov, A., and Williams, E.: Hydration of the lower stratosphere by ice crystal geysers over land convective systems, Atmos. Chem. Phys., 13, 2009.

Khaykin, S., Legras, B., Bucci, S., Sellitto, P., Isaksen, L., Tencé, F., Bekki, S., Bourassa, A., Rieger, L., Zawada, D., Jumelet, J., and Godin-Beekmann, S.: The 2019/20 Australian wildfires generated a persistent smoke-charged vortex rising up to 35 km altitude, Commun Earth Environ, 1, 1–12, https://doi.org/10.1038/s43247-020-00022-5, 2020.

Khaykin, S., Moyer, E., Krämer, M., Clouser, B., Bucci, S., Legras, B., Lykov, A., Afchine, A., Cairo, F., Formanyuk, I., Mitev, V., Matthey, R., Rolf, C., Singer, C., Spelten, N., Volkov, V., Yushkov, V., and Stroh, F.: Persistence of moist plumes from overshooting convection in the Asian monsoon anticyclone, Gases/Field Measurements/Stratosphere/Physics (physical properties and processes), https://doi.org/10.5194/acp-2021-653, 2021.

Khaykin, S. M., Moyer, E., Krämer, M., Clouser, B., Bucci, S., Legras, B., Lykov, A., Afchine, A., Cairo, F., Formanyuk, I., Mitev, V., Matthey, R., Rolf, C., Singer, C. E., Spelten, N., Volkov, V., Yushkov, V., and Stroh, F.: Persistence of moist plumes from overshooting convection in the Asian monsoon anticyclone, Atmospheric Chemistry and Physics, 22, 3169–3189, https://doi.org/10.5194/acp-22-3169-2022, 2022.

Khlopenkov, K. V., Bedka, K. M., Cooney, J. W., and Itterly, K.: Recent Advances in Detection of Overshooting Cloud Tops From Longwave Infrared Satellite Imagery, Journal of Geophysical Research: Atmospheres, 126, e2020JD034359, https://doi.org/10.1029/2020JD034359, 2021.

Kim, J., Randel, W. J., and Birner, T.: Convectively Driven Tropopause-Level Cooling and Its Influences on Stratospheric Moisture, Journal of Geophysical Research: Atmospheres, 123, 590–606, https://doi.org/10.1002/2017JD027080, 2018.

Kim, J.-E. and Alexander, M. J.: Direct impacts of waves on tropical cold point tropopause temperature, Geophysical Research Letters, 42, 1584–1592, https://doi.org/10.1002/2014GL062737, 2015.

Kim, J.-E., Alexander, M. J., Bui, T. P., Dean-Day, J. M., Lawson, R. P., Woods, S., Hlavka, D., Pfister, L., and Jensen, E. J.: Ubiquitous influence of waves on tropical high cirrus clouds, Geophysical Research Letters, 43, 5895–5901, https://doi.org/10.1002/2016GL069293, 2016.

Kim, S.-Y., Chun, H.-Y., and Wu, D. L.: A study on stratospheric gravity waves generated by Typhoon Ewiniar: Numerical simulations and satellite observations, Journal of Geophysical Research: Atmospheres, 114, https://doi.org/10.1029/2009JD011971, 2009.

Korolev, A., McFarquhar, G., Field, P. R., Franklin, C., Lawson, P., Wang, Z., Williams, E., Abel, S. J., Axisa, D., Borrmann, S., Crosier, J., Fugal, J., Krämer, M., Lohmann, U., Schlenczek, O., Schnaiter, M., and Wendisch, M.: Mixed-Phase Clouds: Progress and Challenges, Meteorological Monographs, 58, 5.1-5.50, https://doi.org/10.1175/AMSMONOGRAPHS-D-17-0001.1, 2017.

Krämer, M., Rolf, C., Luebke, A., Afchine, A., Spelten, N., Costa, A., Meyer, J., Zöger, M., Smith, J., Herman, R. L., Buchholz, B., Ebert, V., Baumgardner, D., Borrmann, S., Klingebiel, M., and Avallone, L.: A microphysics guide to cirrus clouds – Part 1: Cirrus types, Atmospheric Chemistry and Physics, 16, 3463–3483, https://doi.org/10.5194/acp-16-3463-2016, 2016.

Krämer, M., Rolf, C., Spelten, N., Afchine, A., Fahey, D., Jensen, E., Khaykin, S., Kuhn, T., Lawson, P., Lykov, A., Pan, L. L., Riese, M., Rollins, A., Stroh, F., Thornberry, T., Wolf, V., Woods, S., Spichtinger, P., Quaas, J., and Sourdeval, O.: A microphysics guide to cirrus – Part 2: Climatologies of clouds and humidity from observations, Atmos. Chem. Phys., 20, 12569–12608, https://doi.org/10.5194/acp-20-12569-2020, 2020.

Kuhn, T. and Heymsfield, A. J.: In Situ Balloon-Borne Ice Particle Imaging in High-Latitude Cirrus, Pure Appl. Geophys., 173, 3065–3084, https://doi.org/10.1007/s00024-016-1324-x, 2016.

Lawson, R. P., Pilson, B., Baker, B., Mo, Q., Jensen, E., Pfister, L., and Bui, P.: Aircraft measurements of microphysical properties of subvisible cirrus in the tropical tropopause layer, Atmospheric Chemistry and Physics, 8, 1609–1620, https://doi.org/10.5194/acp-8-1609-2008, 2008.

Lee, K.-O., Dauhut, T., Chaboureau, J.-P., Khaykin, S., Krämer, M., and Rolf, C.: Convective hydration in the tropical tropopause layer during the StratoClim aircraft campaign: pathway of an observed hydration patch, Atmospheric Chemistry and Physics, 19, 11803–11820, https://doi.org/10.5194/acp-19-11803-2019, 2019.

Leena, P. P., Venkat Ratnam, M., Krishna Murthy, B. V., and Vijaya Bhaskara Rao, S.: Detection of high frequency gravity waves using high resolution radiosonde observations, Journal of Atmospheric and Solar-Terrestrial Physics, 77, 254–259, https://doi.org/10.1016/j.jastp.2012.01.003, 2012.

Li, D., Vogel, B., Müller, R., Bian, J., Günther, G., Ploeger, F., Li, Q., Zhang, J., Bai, Z., Vömel, H., and Riese, M.: Dehydration and low ozone in the tropopause layer over the Asian monsoon caused by tropical cyclones: Lagrangian transport calculations using ERA-Interim and ERA5 reanalysis data, Atmospheric Chemistry and Physics, 20, 4133–4152, https://doi.org/10.5194/acp-20-4133-2020, 2020.

Li, L., Yang, J., Lin, C.-Y., Chua, C. T., Wang, Y., Zhao, K., Wu, Y.-T., Liu, P. L.-F., Switzer, A. D., Mok, K. M., Wang, P., and Peng, D.: Field survey of Typhoon Hato (2017) and a comparison with storm surge modeling in Macau, Natural Hazards and Earth System Sciences, 18, 3167–3178, https://doi.org/10.5194/nhess-18-3167-2018, 2018.

Liou, K.-N.: Influence of Cirrus Clouds on Weather and Climate Processes: A Global Perspective, Monthly Weather Review, 114, 1167–1199, https://doi.org/10.1175/1520-0493(1986)114<1167:IOCCOW>2.0.CO;2, 1986.

Liou, K.-N.: Cirrus clouds and climate, Access Science, https://doi.org/10.1036/1097-8542.YB050210, 2005.

Liou, Y. A., Pavelyev, A. G., Huang, C. Y., Igarashi, K., Hocke, K., and Yan, S. K.: Analytic method for observation of the gravity waves using radio occultation data, Geophysical Research Letters, 30, https://doi.org/10.1029/2003GL017818, 2003.

Lohmann, U. and Gasparini, B.: A cirrus cloud climate dial?, Science, 357, 248–249, https://doi.org/10.1126/science.aan3325, 2017.

Martins, E., Noel, V., and Chepfer, H.: Properties of cirrus and subvisible cirrus from nighttime Cloud-Aerosol Lidar with Orthogonal Polarization (CALIOP), related to atmospheric dynamics and water vapor, Journal of Geophysical Research: Atmospheres, 116, https://doi.org/10.1029/2010JD014519, 2011.

Mitchell, D. L., Rasch, P., Ivanova, D., McFarquhar, G., and Nousiainen, T.: Impact of small ice crystal assumptions on ice sedimentation rates in cirrus clouds and GCM simulations, Geophysical Research Letters, 35, https://doi.org/10.1029/2008GL033552, 2008.

Murphy, D. M. and Koop, T.: Review of the vapour pressures of ice and supercooled water for atmospheric applications, Quarterly Journal of the Royal Meteorological Society, 131, 1539–1565, https://doi.org/10.1256/qj.04.94, 2005.

Nolan, D. S. and Zhang, J. A.: Spiral gravity waves radiating from tropical cyclones, Geophysical Research Letters, 44, 3924–3931, https://doi.org/10.1002/2017GL073572, 2017.

Nützel, M., Podglajen, A., Garny, H., and Ploeger, F.: Quantification of water vapour transport from the Asian monsoon to the stratosphere, Atmospheric Chemistry and Physics, 19, 8947–8966, https://doi.org/10.5194/acp-19-8947-2019, 2019.

Pandit, A. K., Gadhavi, H. S., Venkat Ratnam, M., Raghunath, K., Rao, S. V. B., and Jayaraman, A.: Long-term trend analysis and climatology of tropical cirrus clouds using 16 years of lidar data set over Southern India, Atmospheric Chemistry and Physics, 15, 13833–13848, https://doi.org/10.5194/acp-15-13833-2015, 2015.

Podglajen, A., Plougonven, R., Hertzog, A., and Jensen, E.: Impact of gravity waves on the motion and distribution of atmospheric ice particles, Atmospheric Chemistry and Physics, 18, 10799–10823, https://doi.org/10.5194/acp-18-10799-2018, 2018.

Pun, I.-F., Chan, J. C. L., Lin, I.-I., Chan, K. T. F., Price, J. F., Ko, D. S., Lien, C.-C., Wu, Y.-L., and Huang, H.-C.: Rapid Intensification of Typhoon Hato (2017) over Shallow Water, Sustainability, 11, 3709, https://doi.org/10.3390/su11133709, 2019.

Randel, W. J. and Jensen, E. J.: Physical processes in the tropical tropopause layer and their roles in a changing climate, Nature Geosci, 6, 169–176, https://doi.org/10.1038/ngeo1733, 2013.

Ravindra Babu, S., Venkat Ratnam, M., Basha, G., Krishnamurthy, B. V., and Venkateswararao, B.: Effect of tropical cyclones on the tropical tropopause parameters observed using COSMIC GPS RO data, Atmospheric Chemistry and Physics, 15, 10239–10249, https://doi.org/10.5194/acp-15-10239-2015, 2015.

Ravindrababu, S., Ratnam, M. V., Basha, G., Liou, Y.-A., and Reddy, N. N.: Large Anomalies in the Tropical Upper Troposphere Lower Stratosphere (UTLS) Trace Gases Observed during the Extreme 2015–16 El Niño Event by Using Satellite Measurements, Remote Sensing, 11, 687, https://doi.org/10.3390/rs11060687, 2019.

Reinares Martínez, I., Evan, S., Wienhold, F. G., Brioude, J., Jensen, E. J., Thornberry, T. D., Héron, D., Verreyken, B., Körner, S., Vömel, H., Metzger, J.-M., and Posny, F.: Unprecedented Observations of a Nascent In Situ Cirrus in the Tropical Tropopause Layer, Geophysical Research Letters, 48, e2020GL090936, https://doi.org/10.1029/2020GL090936, 2021.

Rollins, A. W., Thornberry, T. D., Gao, R. S., Woods, S., Lawson, R. P., Bui, T. P., Jensen, E. J., and Fahey, D. W.: Observational constraints on the efficiency of dehydration mechanisms in the tropical tropopause layer, Geophysical Research Letters, 43, 2912–2918, https://doi.org/10.1002/2016GL067972, 2016.

Romps, D. M. and Kuang, Z.: Overshooting convection in tropical cyclones, Geophysical Research Letters, 36, https://doi.org/10.1029/2009GL037396, 2009.

Saito, M., Iwabuchi, H., Yang, P., Tang, G., King, M. D., and Sekiguchi, M.: Ice particle morphology and microphysical properties of cirrus clouds inferred from combined CALIOP-IIR measurements, Journal of Geophysical Research: Atmospheres, 122, 4440–4462, https://doi.org/10.1002/2016JD026080, 2017.

Sakai, T., Nagai, T., Nakazato, M., Mano, Y., and Matsumura, T.: Ice clouds and Asian dust studied with lidar measurements of particle extinction-to-backscatter ratio, particle depolarization, and water-vapor mixing ratio over Tsukuba, Appl. Opt., AO, 42, 7103–7116, https://doi.org/10.1364/AO.42.007103, 2003.

Sanderson, B. M., Piani, C., Ingram, W. J., Stone, D. A., and Allen, M. R.: Towards constraining climate sensitivity by linear analysis of feedback patterns in thousands of perturbed-physics GCM simulations, Clim Dyn, 30, 175–190, https://doi.org/10.1007/s00382-007-0280-7, 2008.

Schoeberl, M., Dessler, A., Ye, H., Wang, T., Avery, M., and Jensen, E.: The impact of gravity waves and cloud nucleation threshold on stratospheric water and tropical tropospheric cloud fraction, Earth and Space Science, 3, 295–305, https://doi.org/10.1002/2016EA000180, 2016.

Schoeberl, M. R., Jensen, E. J., and Woods, S.: Gravity waves amplify upper tropospheric dehydration by clouds, Earth and Space Science, 2, 485–500, https://doi.org/10.1002/2015EA000127, 2015.

Schoeberl, M. R., Jensen, E. J., Pfister, L., Ueyama, R., Wang, T., Selkirk, H., Avery, M., Thornberry, T., and Dessler, A. E.: Water Vapor, Clouds, and Saturation in the Tropical Tropopause Layer, Journal of Geophysical Research: Atmospheres, 124, 3984–4003, https://doi.org/10.1029/2018JD029849, 2019.

Shibata, T., Vömel, H., Hamdi, S., Kaloka, S., Hasebe, F., Fujiwara, M., and Shiotani, M.: Tropical cirrus clouds near cold point tropopause under ice supersaturated conditions observed by lidar and balloon-borne cryogenic frost point hygrometer, Journal of Geophysical Research: Atmospheres, 112, https://doi.org/10.1029/2006JD007361, 2007.

Shibata, T., Hayashi, M., Naganuma, A., Hara, N., Hara, K., Hasebe, F., Shimizu, K., Komala, N., Inai, Y., Vömel, H., Hamdi, S., Iwasaki, S., Fujiwara, M., Shiotani, M., Ogino, S.-Y., and Nishi, N.: Cirrus cloud appearance in a volcanic aerosol layer around the tropical cold point tropopause over Biak, Indonesia, in January 2011, Journal of Geophysical Research: Atmospheres, 117, https://doi.org/10.1029/2011JD017029, 2012.

Smith, J. B., Wilmouth, D. M., Bedka, K. M., Bowman, K. P., Homeyer, C. R., Dykema, J. A., Sargent, M. R., Clapp, C. E., Leroy, S. S., Sayres, D. S., Dean-Day, J. M., Bui, T. P., and Anderson, J. G.: A case study of convectively sourced water vapor observed in the overworld stratosphere over the United States, Journal of Geophysical Research: Atmospheres, 122, 9529–9554, https://doi.org/10.1002/2017JD026831, 2017.

Smith, J. W., Bushell, A. C., Butchart, N., Haynes, P. H., and Maycock, A. C.: The Effect of Convective Injection of Ice on Stratospheric Water Vapor in a Changing Climate, Geophysical Research Letters, 49, e2021GL097386, https://doi.org/10.1029/2021GL097386, 2022.

Solomon, S., Rosenlof, K. H., Portmann, R. W., Daniel, J. S., Davis, S. M., Sanford, T. J., and Plattner, G.-K.: Contributions of Stratospheric Water Vapor to Decadal Changes in the Rate of Global Warming, Science, 327, 1219–1223, https://doi.org/10.1126/science.1182488, 2010.

Stockwell, R. G., Mansinha, L., and Lowe, R. P.: Localization of the complex spectrum: the S transform, IEEE Transactions on Signal Processing, 44, 998–1001, https://doi.org/10.1109/78.492555, 1996.

Sun, N., Fu, Y., Zhong, L., Zhao, C., and Li, R.: The Impact of Convective Overshooting on the Thermal Structure over the Tibetan Plateau in Summer Based on TRMM, COSMIC, Radiosonde, and Reanalysis Data, Journal of Climate, 34, 8047–8063, https://doi.org/10.1175/JCLI-D-20-0849.1, 2021.

Tegtmeier, S., Anstey, J., Davis, S., Dragani, R., Harada, Y., Ivanciu, I., Pilch Kedzierski, R., Krüger, K., Legras, B., Long, C., Wang, J. S., Wargan, K., and Wright, J. S.: Temperature and tropopause characteristics from reanalyses data in the tropical tropopause layer, Atmospheric Chemistry and Physics, 20, 753–770, https://doi.org/10.5194/acp-20-753-2020, 2020.

Thomason, L. and Peter, Th.: SPARC Assessment of Stratospheric Aerosol Properties (ASAP), SPARC Report, SPARC Office, 2006.

Thornberry, T. D., Rollins, A. W., Avery, M. A., Woods, S., Lawson, R. P., Bui, T. V., and Gao, R.-S.: Ice water content-extinction relationships and effective diameter for TTL cirrus derived from in situ measurements during ATTREX 2014, Journal of Geophysical Research: Atmospheres, 122, 4494–4507, https://doi.org/10.1002/2016JD025948, 2017.

Ueyama, R., Jensen, E. J., and Pfister, L.: Convective Influence on the Humidity and Clouds in the Tropical Tropopause Layer During Boreal Summer, Journal of Geophysical Research: Atmospheres, 123, 7576–7593, https://doi.org/10.1029/2018JD028674, 2018.

Vernier, J.-P., Fairlie, T. D., Natarajan, M., Wienhold, F. G., Bian, J., Martinsson, B. G., Crumeyrolle, S., Thomason, L. W., and Bedka, K. M.: Increase in upper tropospheric and lower stratospheric aerosol levels and its potential connection with Asian pollution, Journal of Geophysical Research: Atmospheres, 120, 1608–1619, https://doi.org/10.1002/2014JD022372, 2015.

Vernier, J.-P., Fairlie, T. D., Deshler, T., Natarajan, M., Knepp, T., Foster, K., Wienhold, F. G., Bedka, K. M., Thomason, L., and Trepte, C.: In situ and space-based observations of the Kelud volcanic plume: The persistence of ash in the lower stratosphere, Journal of Geophysical Research: Atmospheres, 121, 11,104-11,118, https://doi.org/10.1002/2016JD025344, 2016.

Vernier, J.-P., Fairlie, T. D., Deshler, T., Ratnam, M. V., Gadhavi, H., Kumar, B. S., Natarajan, M., Pandit, A. K., Raj, S. T. A., Kumar, A. H., Jayaraman, A., Singh, A. K., Rastogi, N., Sinha, P. R., Kumar, S., Tiwari, S., Wegner, T., Baker, N., Vignelles, D., Stenchikov, G., Shevchenko, I., Smith, J., Bedka, K., Kesarkar, A., Singh, V., Bhate, J., Ravikiran, V., Rao, M. D., Ravindrababu, S., Patel, A., Vernier, H., Wienhold, F. G., Liu, H., Knepp, T. N., Thomason, L., Crawford, J., Ziemba, L., Moore, J., Crumeyrolle, S., Williamson, M., Berthet, G., Jégou, F., and Renard, J.-B.: BATAL: The Balloon Measurement Campaigns of the Asian Tropopause Aerosol Layer, Bulletin of the American Meteorological Society, 99, 955–973, https://doi.org/10.1175/BAMS-D-17-0014.1, 2018.

Voudouri, K. A., Giannakaki, E., Komppula, M., and Balis, D.: Variability in cirrus cloud properties using a Polly[XT] Raman lidar over high and tropical latitudes, Atmospheric Chemistry and Physics, 20, 4427–4444, https://doi.org/10.5194/acp-20-4427-2020, 2020.

Wagner, R., Bertozzi, B., Höpfner, M., Höhler, K., Möhler, O., Saathoff, H., and Leisner, T.: Solid Ammonium Nitrate Aerosols as Efficient Ice Nucleating Particles at Cirrus Temperatures, Journal of Geophysical Research: Atmospheres, 125, e2019JD032248, https://doi.org/10.1029/2019JD032248, 2020.

Wang, X., Dessler, A. E., Schoeberl, M. R., Yu, W., and Wang, T.: Impact of convectively lofted ice on the seasonal cycle of water vapor in the tropical tropopause layer, Atmospheric Chemistry and Physics, 19, 14621–14636, https://doi.org/10.5194/acp-19-14621-2019, 2019.

Winker, D. M., Vaughan, M. A., Omar, A., Hu, Y., Powell, K. A., Liu, Z., Hunt, W. H., and Young, S. A.: Overview of the CALIPSO Mission and CALIOP Data Processing Algorithms, Journal of Atmospheric and Oceanic Technology, 26, 2310–2323, https://doi.org/10.1175/2009JTECHA1281.1, 2009.

Wolf, V., Kuhn, T., Milz, M., Voelger, P., Krämer, M., and Rolf, C.: Arctic ice clouds over northern Sweden: microphysical properties studied with the Balloon-borne Ice Cloud particle Imager B-ICI, Atmospheric Chemistry and Physics, 18, 17371–17386, https://doi.org/10.5194/acp-18-17371-2018, 2018.

Woods, S., Lawson, R. P., Jensen, E., Bui, T. P., Thornberry, T., Rollins, A., Pfister, L., and Avery, M.: Microphysical Properties of Tropical Tropopause Layer Cirrus, Journal of Geophysical Research: Atmospheres, 123, 6053–6069, https://doi.org/10.1029/2017JD028068, 2018.

Wu, J. F., Xue, X. H., Hoffmann, L., Dou, X. K., Li, H. M., and Chen, T. D.: A case study of typhoon-induced gravity waves and the orographic impacts related to Typhoon Mindulle (2004) over Taiwan, Journal of Geophysical Research: Atmospheres, 120, 9193–9207, https://doi.org/10.1002/2015JD023517, 2015.

Yorks, J. E., McGill, M. J., Scott, V. S., Wake, S. W., Kupchock, A., Hlavka, D. L., Hart, W. D., and Selmer, P. A.: The Airborne Cloud–Aerosol Transport System: Overview and Description of the Instrument and Retrieval Algorithms, Journal of Atmospheric and Oceanic Technology, 31, 2482–2497, https://doi.org/10.1175/JTECH-D-14-00044.1, 2014.

Young, S. A., Vaughan, M. A., Garnier, A., Tackett, J. L., Lambeth, J. D., and Powell, K. A.: Extinction and optical depth retrievals for CALIPSO's Version 4 data release, Atmospheric Measurement Techniques, 11, 5701–5727, https://doi.org/10.5194/amt-11-5701-2018, 2018.